Waves and Oscillations in Space Plasmas

by

Hiroatsu Sato

Dissertation for the degree of
Philosophiae Doctor

Department of Physics
University of Oslo

September 2011

Series of dissertations submitted to the
Faculty of Mathematics and Natural Sciences, University of Oslo
No. 1137

ISSN 1501-7710

Cover: Inger Sandved Anfinsen.
Printed in Norway: AIT Oslo AS.

Produced in co-operation with Unipub.
The thesis is produced by Unipub merely in connection with the
thesis defence. Kindly direct all inquiries regarding the thesis to the copyright
holder or the unit which grants the doctorate.

To my parents

Acknowledgement

I would like to first express my gratitude to my supervisors Professor Hans Pécseli and Professor Jan Trulsen for their guidance and kind support. They have been encouraging and helping me since my first days in Oslo. It has been a great pleasure for me to work in this project under their patient supervision during these four years.

I gratefully acknowledge technical support given by Bjørn Lybekk, Espen Trondsen and Naoki Kubota at Department of Physics. All the colleagues in Plasma and Space Physics Group have contributed for this work. I have been very fortunate to work with Professor Jøran Moen in FYS 3610 space physics course. Discussions with Dr. Wojciech Miloch and Vegaard Rekaa have been greatly appreciated.

The data for analysis in this thesis originates from ROSE project and their successful experiment. I would like to thank the members of the project for permission to use the rocket data This thesis is supported by PhD fellowship program from University of Oslo. The program has allowed me to attend various inspiring conferences and workshops over Europe.

Last but not least I would like to thank my family and all friends in both Norway and Japan for being always there. I have always charged my energy for life by sharing good time with you all.

Oslo, September 2011
Hiroatsu Sato

Contents

List of Figures

Part I

Electrostatic Waves in Ionospheric Plasmas

Chapter 1

Introduction

Objective of this study

The Earth's near and more distant space environment displays a rich variety of wave phenomena [*Shawhan*, 1979; *Fejer and Providakes*, 1987] that all deserve attention as far as the origin and excitation mechanisms are concerned and also the wave properties themselves. It is for instance found that the arrival of the pressure increase associated with the interplanetary shock driven by an interplanetary coronal mass ejection (ICME) will compress the low latitude geomagnetic field through an intensification of the Chapman-Ferraro magnetopause current. This leads to a sudden impulse (SI) which can be observed also in low latitude magnetometer records. It was demonstrated [*Farrugia and Gratton*, 2011] that such SI-events are generally followed by large amplitude oscillations of ~ 5 min periods. These are observed, for instance, by satellites in the cold, dense magnetosheath and in the hot and tenuous magnetosphere plasmas, consistent with other related observations [*Plaschke et al.*, 2009]. It has also been found [*Kivelson et al.*, 1984; *Sibeck et al.*, 1989; *Korotova and Sibeck*, 1995] that magnetic pulsations with $8-10$ min periods measured by geosynchronous satellites are well correlated with oscillations in the solar wind dynamic pressure.

Other types of waves and oscillations are found in different parts of the magnetosphere and ionosphere of the Earth. The present summary gives particular attention to some basic properties of a very common ionospheric instability [*Bowles et al.*, 1963; *Farley*, 1963; *Buneman*, 1963], where the free energy is found in a large-scale, quasi-stationary electric field. This Farley-Buneman instability is driven by the Hall-current in the collisional plasma typically found in the ionospheric E-region in the equatorial as well as the polar ionospheres, although the *origin* of this electric field is generally

different in the two regions. With $\Omega_{ci} \leq \nu_{ni}$ and $\omega_{ce} \gg \nu_{ne}$, with electron and ion cyclotron frequencies ω_{ce} and Ω_{ci}, while the electron and ion neutral collision frequencies are ν_{ne} and ν_{ni}, respectively, we have the ions to be effectively dragged by the neutrals while the electrons on the other hand are moving approximately with the $\mathbf{E}_0 \times \mathbf{B}_0/{B_0}^2$-velocity.

The present summary outlines some of the elements entering the analysis of rocket data. Details can be found in the enclosed papers and other publications, in particular concerning the magnetospheric oscillations.

Chapter 2

Farley-Buneman and Gradient Instabilities

2.1 Fluid Model and Dispersion Relation

A simplified fluid model and dispersion relation can be obtained in the limit where the ion-neutral collisions are frequent, meaning $\Omega_{ci} \leq \nu_{in}$ while the electrons in comparison are experiencing few collisions $\omega_{ce} \gg \nu_{en}$. This limit is found in the ionospheric E-region, where the electron component is drifting with a velocity close to the $\mathbf{E}_0 \times \mathbf{B}_0/B_0^2$-drift velocity. The ion component is on the other hand almost at rest in the neutral gas frame of reference (which might be moving due to neutral winds).

The derivation of the general dispersion relation starts with following basic fluid equations [*Farley*, 1963; *Buneman*, 1963; *Fejer et al.*, 1984]

Continuity equation for the electron and the ion,

$$\frac{\partial N}{\partial t} + \nabla \cdot (N\boldsymbol{V}) = Q - \beta_r N^2$$

Equation of motion for both species

$$m\frac{D\boldsymbol{V}}{Dt} = q(-\nabla\phi + \boldsymbol{V} \times \boldsymbol{B}) - \frac{\nabla P}{N} - m\nu\boldsymbol{V}$$

and Poisson equation

$$\nabla^2\phi = \frac{e(N_e - N_i)}{\varepsilon_0}$$

The common notation N, V and P are fluid specie's density, velocity and pressure while D/Dt is the convective derivative. These general equations include effect from production Q and recombination rates β_r We consider linear perturbations and inserr them into the first order equations. The fluctuations introduced here have the plane waveform characterized as $exp[i(\boldsymbol{k}\cdot\boldsymbol{r}-\omega t)]$ We only consider waves travelling primarily in field aligned direction($k_\perp \gg k_\parallel$). We also assume quasi-neutrality and focus on the waves which have scale size much larger than the Debye length. This assumption allows us to consider wavelength larger than probe separation in rocket research in the ionosphere.

After these analysis the general dispersion relation reduces to

$$(\omega + i2\beta_r N_0) - \boldsymbol{k}\cdot\boldsymbol{V_d} + [(\omega + i2\beta_r N_0)(\nu_i - i\omega) + ik^2 {C_s}^2]\left(\frac{\psi}{\nu_i} - \frac{i}{kL_N\Omega_i}\right) = 0$$

where the plasma density gradient is L_N. The corresponding oscillation frequency and the growth rate are

$$\omega_r = \frac{kV_d cos\beta_r}{1+\psi},$$

$$\omega_i = \frac{1}{1+\psi}\left[\frac{\psi}{\nu_{in}}(\omega^2 - k^2C_s^2) + \frac{\omega_r\nu_i}{kL_N\Omega_i}\right] - 2\alpha N_0,$$

where β_r is a recombination coefficient and

$$\psi = \frac{\nu_{en}\nu_{in}}{\omega_{ce}\Omega_{ci}}\left(1 + \frac{\omega_{ce}^2 k_\parallel^2}{\nu_e^2 k^2}\right).$$

The foregoing analysis implies a simplifying assumption of small growth rates, i.e. $\omega_r \ll \omega_i$.

2.2 Conditions for Unstable Waves

Gradient instability

Conceptually, the gradient instability is very similar to the Rayleigh–Taylor instability discussed elsewhere [*Chen*, 1984]. The similarity can be made evident by considering Fig. 2.1. Due to their small mobility, caused by large collision frequencies $\nu_i \gg \Omega_c$, the ions are almost immobile. The electrons on

the other hand are assumed to drift with essentially the local $\mathbf{E}_0 \times \mathbf{B}$–velocity, apart from small corrections of the order of ν_e/ω_c. A small initial perturbation gives rise to polarization electric fields which enhance the perturbation (instability) if $\mathbf{E}_0 \cdot \nabla n_0 > 0$. Depending on point of view, it can be argued that on the other hand a gradient in plasma density has a stabilizing effect on the Farley–Buneman instability when $\mathbf{E}_0 \cdot \nabla n_0 < 0$ since the wave–growth due to the Farley–Buneman instability is diminished by the damping due to the gradient in this case.

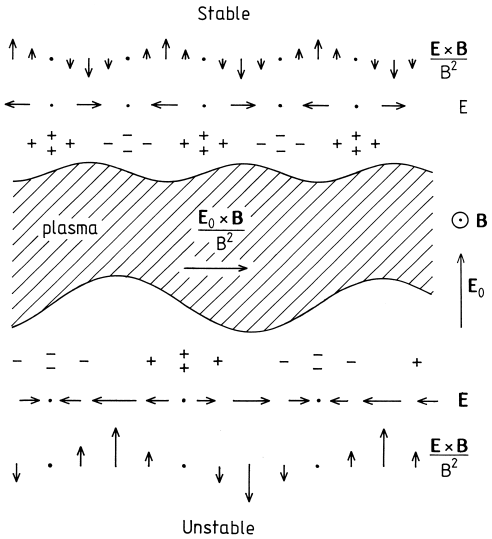

Figure 2.1: Geometry for a simple description of the gradient instability of a plasma with neutral collisions and an externally imposed dc–electric field. $\mathbf{E}_0$ is the macroscopic "external" electric field, which is here taken to be constant in space, while $\mathbf{E}$ is a space-time varying perturbation.

The growth rate of Farley-Buneman wave

The imaginary part of the frequency contains essentially three terms:

i) a recombination term which always gives damping. This damping originates in the loss of wave momentum by recombination. When new ions

and electrons are created by ionization to replace those being lost, these new particles have to receive momentum in order to participate in the organized wave-motion, and the corresponding energy has to be taken from the wave itself.

ii) a purely gradient depending term, i.e. the second one in the angular brackets, which depending on the sign of L_N contributes to an instability or a damping.

iii) the first term in the angular brackets gives instability if ${\omega_r}^2 > {k_y}^2 {C_s}^2$. This instability can be present also for vanishing density gradients, $L \to \infty$. In this limit the plasma becomes unstable essentially when the electron drift across the magnetic field lines exceeds the ion acoustic sound velocity. This is the instability often called the Farley–Buneman instability after the two scientist who discovered it simultaneously [*Farley*, 1963; *Buneman*, 1963], or the type I irregularity after the classification used in describing radar backscattering from the ionosphere [*Rogister and D'Angelo*, 1970]. The Farley-Buneman instability is due to ion inertia, while the gradient instability is recovered also when ion inertial effects are ignored and the ion motion described by a simple mobility term.

It is important that the foregoing arguments rely on the assumption of small growth-rates, i.e. the results are valid close to threshold. For general conditions the dispersion relation should be solved numerically. Also the approximation $n_0'/n_0 \approx 1/L_N$ =const. deserves some attention here. For large wavenumbers, i.e. short wavelengths this local approximation will often be adequate. However, the full dispersion relation is particularly sensitive to the long wavelength-limit, and here an approximation of a locally exponential density gradient will usually be difficult to justify. A complete understanding of this long wavelength-limit requires a solution of the full eigenvalue problem. Such an analysis is, unfortunately, rather complicated in general, and it is seldom carried out.

The ionospheric waves described here have been extensively studied by radar and by in-situ rocket measurements [*Pfaff et al.*, 1984, 1985; *Rose et al.*, 1992; *Pfaff et al.*, 1997; *Jackel et al.*, 1997; *Iranpour et al.*, 1997]. Some of the results are summarized by *Kelley* [1989]. Seemingly, the first observations were made by *Olesen and Rybner* [1958] by radar scattering.

Chapter 3

Electric Field Data

3.1 The Rose Project

During the ROSE rocket campaign [*Rose et al.*, 1992; *Rinnert*, 1992], an instrumented payload F4 was launched in February 1989 from Kiruna, Sweden. The peak altitude of this flight was approximately 125 km. Good quality data were obtained on the up-leg as well as on the down-leg parts of the flight with approximately 20 km horizontal separation in the E-region. The DC-electric field strength was changing during the flight (typically $E_0 \approx 40$ mV/m up-leg, and $E_0 \approx 60$ mV/m down-leg), so in reality we have data from two independent experiments. (Related numerical studies of *Dyrud et al.* [2008] use the maximum peak value of $E_0 \approx 70$ mV/m to emphasize the nonlinear features.) A summary of our previous results from studies of these data are given by *Krane et al.* [2010].

Objective of the project

One of the main objectives of the Rose rocket campaign was to obtain data for the large scale DC-electric fields $\mathbf{E}_0$ in the ionosphere and the basic plasma parameters, such as the altitude variation of the density. The electron and ion temperature measurements gave only qualitative results, but measurements of the neutral gas density and temperature [*Friker and Lübken*, 1992] indicated a neutral temperature of 218 ± 5 K, which can be used as an approximation to the ion temperature.

The detectors on the rockets, see Figure 3.1 and 3.2, allow also analysis of low frequency fluctuations, up to 1 kHz. The original Nyquist frequency of the datasampling was 2 kHz, but due to some filters in the amplifiers etc., the effective bandwidth was below 1 kHz. Consequently, the data were reduced

by adding samples together two-by-two to reduce the Nyquist frequency, without loss of relevant information. In Figure 3.3 we show results for the DC-electric fields detected by the ROSE4 rocket on both upleg and downleg parts of the flight. The analysis takes care to remove the $\mathbf{V} \times \mathbf{B}_0$-induced electric fields, where $\mathbf{V}$ is the rocket velocity vector. For studies of fluctuations, we remove the slowly varying parts of the electric field, using a filter that removes frequencies below the rocket spin frequency (approximately 2 Hz) and it first few harmonics.

Figure 3.1: The Rose sounding rocket. Photo is taken during mounting.

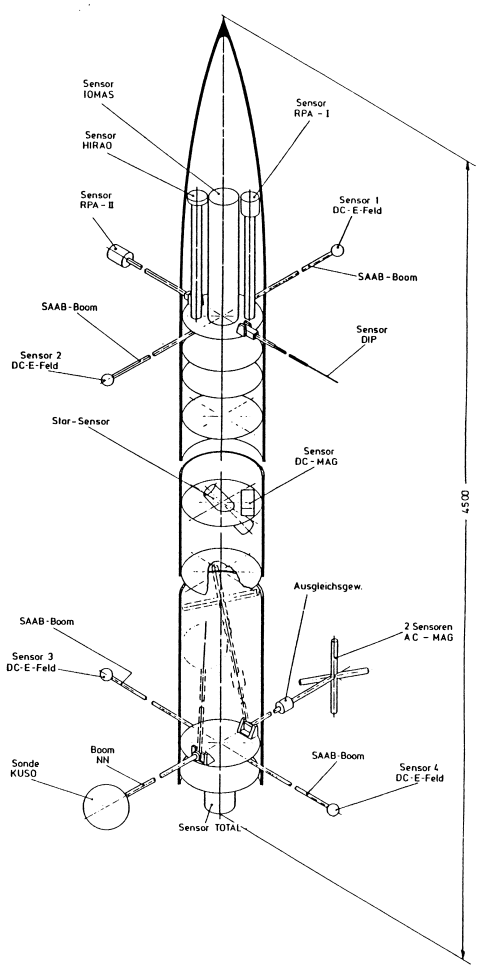

Figure 3.2: Schematic illustration of the configuration of the probes on the Rose rocket, figure taken from *Rose et al.* [1990]

Rose Rocket and Electric Field Experiment

The ionospheric conditions and details of the instrumentation relevant for the present data-set were discussed in a special issue of *Journal of Atmospheric and Terrestrial Physics* (*54*, 655-818, 1992) and also in a detailed report [*Rose et al.*, 1990]. For completeness we here summarize some of the basic parameters of the flight. The ROSE F4 rocket was launched in a direction perpendicular to the Hall current of the electrojet. The spin period of the rocket was approximately 0.5 s. The corresponding time for the coning motion was approximately 6 s with cone-angle approximately 2°. The ELF signals analyzed were obtained by gold-plated spherical probes of 5 cm diameter [*Rinnert*, 1992], mounted on two pairs of booms, one near the top of the payload (labeled 1 and 2) and the other 185 cm lower (labeled 3 and 4), oriented at an angle of 90° with respect to the first pair, as illustrated in Figure 3.2. The length of each boom was 180 cm measured from the rocket center, giving a probe separation of 360 cm on each boom. The following analysis assumes that the booms and probes are positioned in this ideal geometry also after launch, ignoring also possible vibrations in the booms.

3.2 Electrostatic Waves Observed in the Ionospheric E-region

We analyzed the fluctuating signals $U_6(t) = \phi_1(t) - \phi_2(t)$; $U_5(t) = \phi_4(t) - \phi_3(t)$; $U_4(t) = \phi_1(t) - \phi_4(t)$; $U_3(t) = \phi_2(t) - \phi_3(t)$; $U_2(t) = \phi_1(t) - \phi_3(t)$; and $U_1(t) = \phi_2(t) - \phi_4(t)$, where $\phi_j(t)$ for $j = 1, 2, 3, 4$ denotes the potential on the j-th probe with respect to a suitably defined common ground. There is a redundancy in the available signals, which can be used to check the performance of individual probes. For wavelengths much larger than the probe separations, the potential difference signals can be used to estimate the fluctuating electric fields, $\widetilde{\mathbf{E}}$. The signals were digitized with 12 bit resolution. The space-time varying electric field fluctuations were sampled at a time interval of 0.5 ms, giving a Nyquist frequency of 1000 Hz. The electric circuits give an effective frequency limitation closer to 600 Hz. The DC-electric field $\mathbf{E}_0$ was measured by the same probes. The altitude variation of the DC-plasma density is shown in Figure 3.5, here redrawn from *Rose et al.* [1990].

Studies of the ROSE F4 data demonstrated that a broad band spectrum of low frequency electrostatic waves propagate in the $\mathbf{E}_0 \times \mathbf{B}_0$-direction with phase velocities in the range of $250 - 400$ m/s as shown by *Iranpour*

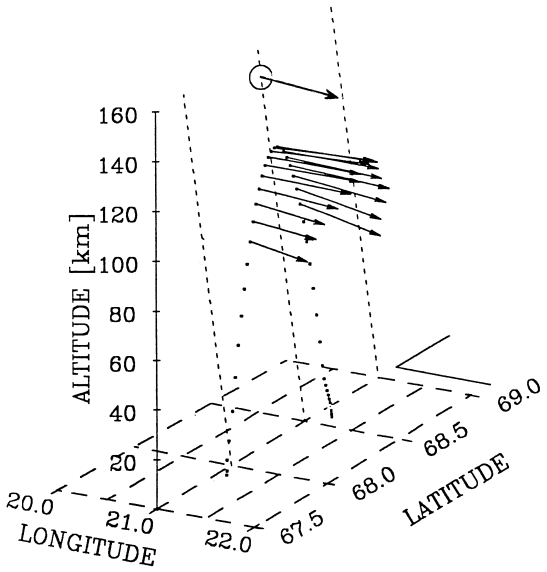

Figure 3.3: DC $\mathbf{E}\times\mathbf{E}$-drift velocities deduced from the electric field data obtained by the Rose4 Rocket.

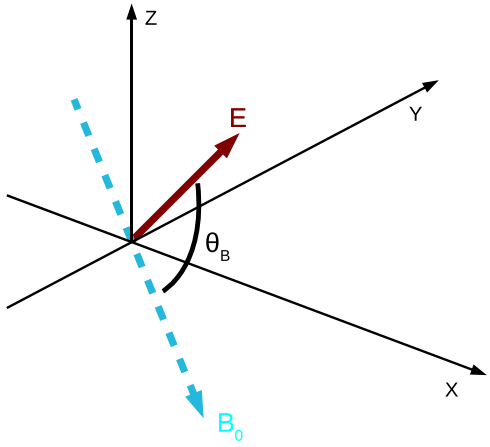

Figure 3.4: Schematic display of geomagnetic vector B_0 and fluctuating electric field vector E in three dimensional space.

et al. [1997], *Krane et al.* [2000] and *Dyrud et al.* [2006]. The local cross-correlations of data from one of the Greenland rockets with RMS-fluctuation levels of 4-8 mV/m, as presented by *Pécseli et al.* [1993] also show a similar magnitude and altitude variation of the propagation velocity, although these features were not discussed in that paper.

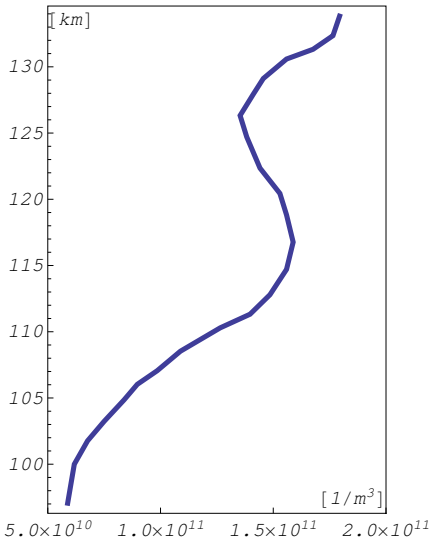

Figure 3.5: Electron density data [*Rose et al.*, 1990]

The observed frequency range on the ROSE F4 rocket is $5 - 1000$ Hz, implying wavelengths in the range of $0.25 - 80$ m. The shortest wavelengths are strongly filtered by the two-point probe sampling of the electrostatic field [*Kelley and Mozer*, 1973; *Pfaff et al.*, 1984; *Krane et al.*, 2000]. The data can thus approximate the fluctuating electric fields only for wavelengths significantly exceeding the probe separation (see Figure 3.2), here corresponding to frequencies below 28 Hz, approximately. We filter the data correspondingly, and consider only a limited spectral range. (In previous related studies by *Rinnert* [1992], the speed of propagation was not known, and too short wavelengths were included in the data analysis.) We filter the data with a band-pass filter $\{8 : 28\}$ Hz, whereby we at the same time remove the rocket spin frequency and its first harmonics, and also ensure that the filter-bandwidth

is larger than the average filter-frequency. (For narrow filter bandwidths, it will be this bandwidth that determines the time variability of the signal output.) In Figure 3.6 we show variations of the electric field vector with time: the arrows represent the magnitude and direction of the local electric field vectors at times after launch.

The electric fields are detected in the frame of the moving and spinning rocket. To obtain the direction in the fixed frame results, the data are transformed to a fixed ground frame, with the z-axis parallel to the ambient magnetic field. The transformation is performed by using the proper rotation matrices.

3.3 Coordinate System

Inertial reference frame

The inertial frame has it's x-axis in the direction of the vernal equinox (VE) and the z-axis pointing towards the celestial north pole (NP). The y-axis is chosen as to complete an orthogonal right hand system.

Rocket reference frame

The x-axis of the body frame is pointing along the major axis of minimum moment of inertial, also called the "spin" axis S. The y-axis is defined by being orthogonal both to x and the star sensor optical axis complete a right hand orthogonal triad. E filed system to body frame system (star sensor) is

$$E'_x = E_x$$
$$E'_y = -E_y$$
$$E'_z = -E_z$$

3.4 Attitude Definition

The transformation from inertial to body coordinates (and vice versa) is defined through five successive rotations by the angles.

RA = right ascension of the angular momentum vector H
DE = declination of H
CRA =coning rotation angle with respect to H

CA = coning (half-) angle
BRA = body rotation angle with respect to the "spin" axis S.

Starting with Rocket frame electric field vector $X_R = (E'_x, E'_y, E'_z)$ one arrives to the inertial frame vector $X_l = (E''_x, E''_y, E''_z)$ with the following transformation

$$X_l = T_{RA} T_{DB} T_{CRA} T_{CA} T_{BRA} X_R$$

where the transformation matrices are defined as follows

$$T_{RA} = \begin{pmatrix} \cos(RA) & -\sin(RA) & 0 \\ \sin(RA) & \cos(RA) & 0 \\ 0 & 0 & 1 \end{pmatrix}, \qquad T_{DE} = \begin{pmatrix} \cos(DE) & 0 & \sin(DE) \\ 0 & 1 & 0 \\ \sin(DE) & 0 & \cos(DE) \end{pmatrix},$$

$$T_{CRA} = \begin{pmatrix} 1 & 0 & 0 \\ 0 & \cos(CRA) & -\sin(CRA) \\ 0 & \sin(CRA) & \cos(CRA) \end{pmatrix}, \quad T_{CA} = \begin{pmatrix} \cos(CA) & 0 & -\sin(CA) \\ 0 & 1 & 0 \\ \sin(CA) & 0 & \cos(CA) \end{pmatrix},$$

$$T_{BRA} = \begin{pmatrix} 1 & 0 & 0 \\ 0 & \cos(BRA) & -\sin(BRA) \\ 0 & \sin(BRA) & \cos(BRA) \end{pmatrix}$$

To transform the electric fields from the rotating rocket frame to the fixed ground frame of reference we have analytical expression for the time variations of CRA, BRA, etc. This information was obtained by the group carrying out the ROSE experiments and have the form of polynomial fits to the observed spin frequency, coning frequency, etc.

The final change of frame that brings the z-axis to be parallel to $\mathbf{B}_0$ are obtained by two rotations. The rotation around z''-axis for

$$\alpha = 136.29^\circ + 21.23^\circ = 157.52^\circ$$

is done by

$$\begin{pmatrix} E_x''' \\ E_y''' \\ E_z''' \end{pmatrix} = \begin{pmatrix} \cos(\alpha) & -\sin(\alpha) & 0 \\ \sin(\alpha) & \cos(\alpha) & 0 \\ 0 & 0 & 1 \end{pmatrix} \begin{pmatrix} E_x'' \\ E_y'' \\ E_z'' \end{pmatrix}$$

Now y''' axis is east, x''' is south. The rotation around y''' axis with

$$\beta = 90^\circ - 68.03^\circ + 12.4^\circ = 34.47^\circ$$

is given by

$$\begin{pmatrix} {E_x}^* \\ {E_y}^* \\ {E_z}^* \end{pmatrix} = \begin{pmatrix} \cos(\beta) & -\sin(\beta) & 0 \\ \sin(\beta) & \cos(\beta) & 0 \\ 0 & 0 & 1 \end{pmatrix} \begin{pmatrix} {E_x}''' \\ {E_y}''' \\ {E_z}''' \end{pmatrix}$$

Now

$${E_x}^* \text{ is south } \perp B_0$$
$${E_y}^* \text{is east } \perp B_0$$
$${E_z}^* \text{ is up } \parallel B_0$$

In Figure 3.6 we show a data sample of electric fields in the fixed ground frame of reference.

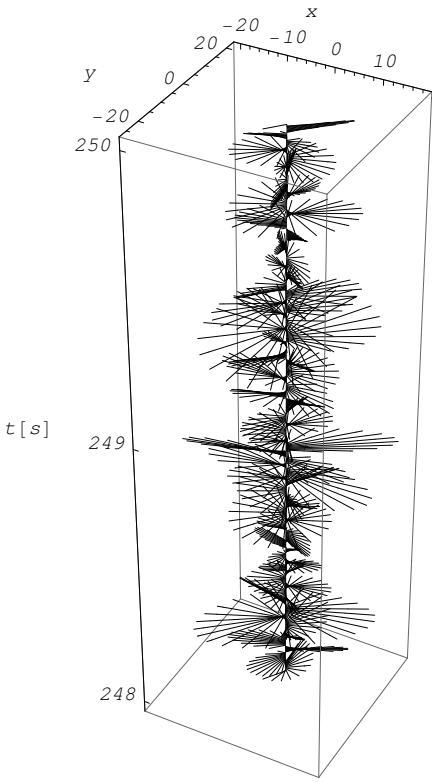

Figure 3.6: A substet of rocket data showing fluctuating electric field. The z-axis is set to be running parallel to local magnetic field.

Chapter 4

Analysis of the Electric Field Data

4.1 Theoretical Background of Intermittency in Signals

One of the most often used words in turbulence is "intermittency". The term is often used to describe that turbulent energy dissipation occurs in localized spatial regions, or "hot spots". More generally, the word "intermittent" is supposed to cover anything of bursty nature. Meteorologists use the word *gust* for sudden increases in wind speed, but the meaning is more or less the same. The concept is thus rather vague, and in reality what we need is a definition of what is *not* an intermittent signal. A somewhat pragmatic definition of intermittency was given by *Rollefson* [1978], stating that "a variable with zero mean will be called intermittent if it has a probability distribution such that extremely small and extremely large excursions are more likely than in a normally distributed variable". In this sense, a random Gaussian process serves as the reference non-intermittent case. It is of course possible to find many types of signals with distributed large and small amplitude regions.

A complete discussion of the statistical distribution of excursions in a random signal (such as the velocity or the electric field magnitude) is very complicated. Analytical forms for the duration of times spent by such a signal at amplitudes exceeding some selected levels were discussed by *Rice* [1945], but the practical applicability of the results is restricted to short times. Some useful estimates can, however, be obtained by simpler means [*Kristensen et al.*, 1991].

Considering a stationary random process $\Phi(t)$, which can represent the electric field magnitude or any other similar scalar process as well, we assume that the amplitude probability density is given as $P(\Phi)$. There are no restriction such as $\langle\Phi\rangle = 0$. Given a long time interval of duration $\mathcal{T}$, the time spent above a given reference level A is then

$$\Theta(A) = \mathcal{T} \int_A^\infty P(\Phi) d\Phi. \tag{4.1}$$

This result can, however, be obtained in many different ways, many short excursions above A or just a few, but long ones, for instance. To find the average number of excursion in the interval $\mathcal{T}$ we need to know also the distribution of the time derivative $d\Phi(t)/dt \equiv \Phi'$ of the signal [*Rice*, 1945; *Bendat*, 1958], i.e. the joint probability density $P(\Phi, \Phi')$. The assumed time-stationarity of the process becomes essential here by implying that $P(\Phi, \Phi')$ is independent of time.

First we note that the time it takes for the signal to cross a small interval $d\Phi$ is given as $d\Phi/\Phi'$. This result is most easily understood if we for the sake of argument consider the signal being a spatial displacement and its derivative then being the velocity.

The fraction of time spent by the signal in an interval dt around a set of amplitudes and time derivatives $\{\Phi, \Phi'\}$ within a narrow interval $d\Phi d\Phi'$ is $P(\Phi, \Phi')d\Phi d\Phi' dt$. For given Φ' the number of crossings of some signal level Φ within dt is consequently [*Bendat*, 1958]

$$\frac{P(\Phi, \Phi')d\Phi d\Phi' dt}{d\Phi/\Phi'} = \Phi' P(\Phi, \Phi')d\Phi' dt\,.$$

The average number $\mathcal{N}$ of upward crossings of the level $\Phi = A$ in the time-interval $\mathcal{T}$ is then obtained by integration with respect to time, which becomes simple since $P(\Phi, \Phi')$ is independent of time, and then with respect to all positive values of Φ'. The results is

$$\mathcal{N}(A) = \mathcal{T} \int_0^\infty \Phi' P(A, \Phi') d\Phi'\,. \tag{4.2}$$

An estimate (and not an accurate result) [*Kristensen et al.*, 1991] for the time spent in excess of a selected signal level $\Phi = A$ is then given by dividing all the time spent spent with $\Phi \geq A$ with the average number of upward crossings giving

$$\frac{\Theta(A)}{\mathcal{N}(A)} = \frac{\int_A^\infty P(\Phi) d\Phi}{\int_0^\infty \Phi' P(A, \Phi') d\Phi'}\,, \tag{4.3}$$

independent of $\mathcal{T}$. In the limit of $A \to -\infty$ we find $\Theta(A)/\mathcal{N}(A) \to \infty$ since we have $P(A \to -\infty, \Phi') \to 0$. For $A \to -\infty$ the entire (infinitely long) record will exceed the reference level.

Note that (4.3) is merely an estimate, obtained by taking an average time spent above a reference level and dividing it by an average time of level crossings. This is not the exact results for average of the time intervals spent over the reference. There are reasons to expect the estimate to be accurate, but it was found worthwhile to test the hypothesis (4.3) on a dataset where the statistical properties are know. This analysis is presented in the appendix to one of the papers attached to the present thesis.

In general we have no a priory knowledge of $P(\Phi, \Phi')$, except from the fact that Φ and Φ' are uncorrelated, since $\langle(\Phi(t) - \langle\Phi\rangle)d\Phi/dt\rangle = \frac{1}{2}d\langle\Phi(t)2\rangle/dt = 0$, since $\langle\Phi'\rangle = 0$. This lack of correlation does not generally imply that Φ and Φ' are statistically independent. Experimental estimate for the joint Probability Density Function $P(|E|, d|E|/dt)$ is showing in Figure 4.1 and 4.2.

Figure 4.3 and 4.4 show intermittent features of the observed turbulence which is one of the major results in this analysis. The solid line gives relationship between varying threshold levels and variation of average time $\langle\Delta T\rangle$ spent above the thresholds. The maximum value $|E|_m$ in the record is used as a reference to measuare the thresholds. A dotted line gives the results obtained for a Gaussian random process with the average and standard deviations for $|E|_m$. A significant deviations from the Gaussian case is clearly seen along the $|E|_m$-field threshold levels in Figure 4.3. In particular there is an excess of time intervals spent over large andl small threshold values as compared to the Gaussian limit. For intermediate threshold level of 10 - 30% of the maximum $|E|_m$, we find noticeably shorter excess time-intervals as compared to the Gaussian reference.

The Gaussian limit

In the non-intermittent Gaussian limit, the signal amplitude Φ and its time derivative Φ' are statistically independent for stationary random processes. We can write the joint probability density as a product $P(\Phi, \Phi') = P(\Phi)P(\Phi')$, where

$$P(\Phi) = \left(\frac{1}{\sqrt{2\pi\sigma^2}}\right) \exp\left(-\frac{1}{2}\frac{(\Phi - \langle\Phi\rangle)^2}{\sigma^2}\right)$$

and

$$P(\Phi') = \left(\frac{1}{\sqrt{2\pi\sigma'^2}}\right) \exp\left(-\frac{1}{2}\frac{\Phi'^2}{\sigma'^2}\right) .$$

For this particular case we have Φ and Φ' to be statistically independent. The standard deviations σ^2 and σ'^2 of the two signals Φ and Φ' are most easily related by the power spectrum $G(\omega)$ of $\Phi(t)$, where we have $\sigma^2 = \int_0^\infty G(\omega)d\omega$ and $\sigma'^2 = \int_0^\infty \omega^2 G(\omega)d\omega$ for stationary Gaussian random processes. In this "non-intermittent limit" we find the relatively simple result

$$\frac{\Theta(A)}{\mathcal{N}(A)} = \pi\frac{\sigma}{\sigma'}\exp\left(\frac{1}{2}(A-\langle\Phi\rangle)^2/\sigma^2\right) \times \operatorname{erfc}\left(\frac{1}{\sqrt{2}}(A-\langle\Phi\rangle)/\sigma\right) . \tag{4.4}$$

where $\operatorname{erfc}(x) \equiv (2/\sqrt{\pi})\int_x^\infty \exp(-\xi^2)d\xi$ is the complementary error function. For $A \to -\infty$ we find also here that $\Theta(A)/\mathcal{N} \to \infty$.

For very large positive excursions, $A - \langle\Phi\rangle \gg \sigma$ the result (4.4) becomes particularly simple [*Kristensen et al.*, 1991], giving

$$\frac{\Theta(A)}{\mathcal{N}(A)} \approx \sqrt{2\pi}\frac{\sigma}{\sigma'}\frac{\sigma}{A-\langle\Phi\rangle} ,$$

implying that the average duration of an excursion is inversely proportional to deviations from the mean value.

It should be mentioned that the statistical analysis of large excursions can be formulated in a slightly different way in terms of extremum distributions, here in terms of the distribution of local maxima [*Bendat*, 1958; *Kristensen et al.*, 1991]. Intermittent features can also be revealed by a conditional data analysis that has been successfully applied also in studies of plasma turbulence [*Johnsen et al.*, 1987]. The Gaussian reference is shown by dotted line in Figure 4.3.

4.2 About Intermittency

The study of the structure functions associated with the fluctuating velocity is an important tool to characterize turbulence of neutral incompressible flows. It is well known [*Chandrasekhar*, 1957] that the second order structure function, as a function of spatial separations, can be obtained by simple dimensional arguments, apart from a numerical constant. For the longitudinal second order velocity structure function in the universal Kolmogorov-Oubokhov range of homogeneous isotropic turbulence we thus find

$$\Psi_2(r) \equiv \left\langle (u_\parallel(0) - u_\parallel(\mathbf{r}))2\right\rangle = C_2(r\epsilon)^{2/3} , \tag{4.5}$$

in terms of the energy dissipation per unit mass ϵ and a universal Kolmogorov constant C_2 which is experimentally found to be in the range $2.1 - 2.5$.

In Eq. (4.5), the notation $_\parallel$ indicates the velocity component parallel to the separation vector $\mathbf{r}$. The result in Eq. (4.5) has found extremely solid experimental support [*Hinze*, 1975]. One could attempt to model higher order structure functions by similar arguments, finding trivially that

$$\Psi_n \equiv \left\langle |u_\parallel(0) - u_\parallel(\mathbf{r})|^n \right\rangle = C_n (r\epsilon)^{n/3} .$$

Experiments demonstrate, however, that for $n > 3$, this analytical result no longer agree with observations, the deviations becoming more and more pronounced with increasing n. The explanation is found in the intermittent nature of turbulence, implying that energy is dissipated in concentrated "spots" or localized regions of space [*Hinze*, 1975; *Anselmet et al.*, 1984].

The universal scaling law given by Eq. (4.5) is reflected also in the turbulent power spectrum of the velocity fluctuations, as expressed in the Kolmogorov-Oubokhov spectrum, which is given as $\epsilon^{2/3} k^{-5/3}$ apart from a universal constant. Since power spectra are easily obtained by spectrum analyzers, many studies prefer to use this representation for studying turbulence in fluids [*Hinze*, 1975] as well as plasmas [*Chen*, 1965; *Pécseli et al.*, 1983; *Krane et al.*, 2000].

The first observations and discussion of intermittency effects seemingly originate from studies of fluid turbulence. The basic ideas will apply also for plasma turbulence and many studies have been carried out, numerically as well as experimentally. Magneto-hydrodynamic (MHD) turbulence in the solar wind has been reported by *Tu and Marsch* [1995] and by *Bruno and Carbone* [2005]. MHD turbulence is in a sense more complicated than its counterpart in incompressible flows since in plasmas generally *two* vector quantities are involved, the magnetic field and the plasma flow velocity. A plasma can however also support a simpler form of wave phenomena: electrostatic waves, which can be adequately described by the space-time variation of a scalar quantity, the electrostatic potential. Such waves are often spontaneously excited in nature by plasma instabilities and have been frequently observed also in the Earth's ionosphere. Intermittency effects have been studied in the ionospheric plasma by, for instance, *Tam et al.* [2005], where their work refers to $\sim$ 700 km altitudes. Other relevant studies of space plasma turbulence can be found in the work by *Chang and Wu* [2008]. In fusion plasma studies it has bee found that intermittency effects are often related to anomalous turbulent transport [*Boedo et al.*, 2003; *Xu et al.*, 2005], an observation also supported by earlier laboratory studies [*Huld et al.*, 1991]. Intermittency effects have been recognized in several different laboratory plasma devices also by e.g. *Fredriksen et al.* [2003] and *Kervalishvili et al.* [2008]. The analysis is not necessarily based on structure functions.

Conditional sampling methods have been used, for example [*Johnsen et al.*, 1987].

The present study applies a somewhat different approach to quantify intermittency effects where we follow ideas suggested by *Kristensen et al.* [1991].

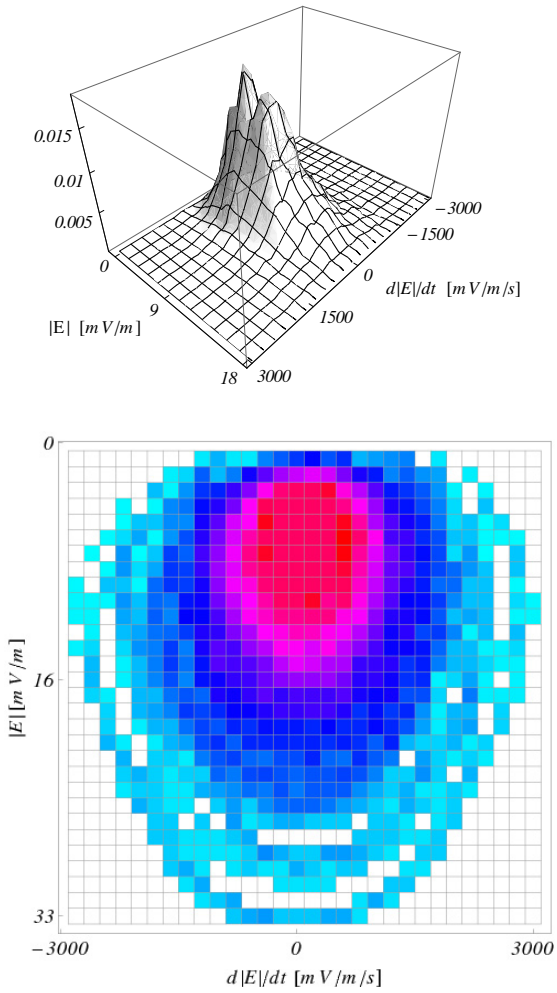

Figure 4.1: Experimental estimate for the joint Probability Density Function $P(|E|, d|E|/dt)$ for DOWN leg condition. The upper figure is surface plot and contour plot to the bottom.

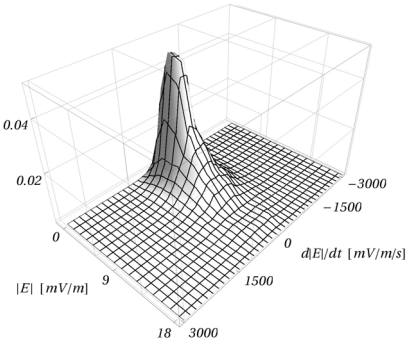

Figure 4.2: Experimental estimate for the joint Probability Density Function $P(|E|, d|E|/dt)$ for UP leg condition.

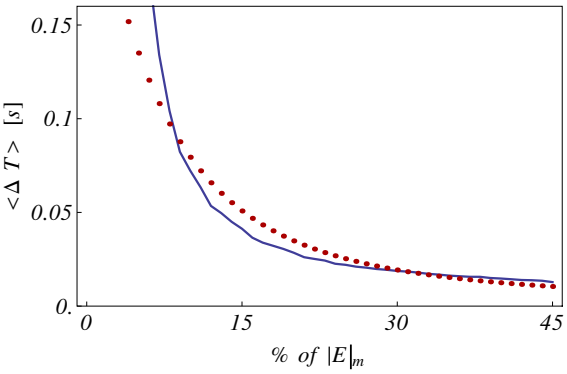

Figure 4.3: Average time interval $\langle \Delta T \rangle$ spent above the varying threshold levels of the maximum value $|E|_m$. Full line shows recorded data and the dotted line is result from Gaussian random process.

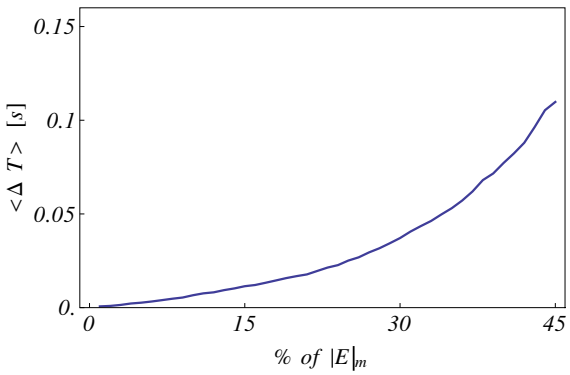

Figure 4.4: Average time interval $\langle \Delta T \rangle$ spent below the varying threshold levels of the maximum value $|E|_m$.

Chapter 5

Summary of Papers

Paper 1:
Minute-scale period oscillations of the magnetosphere, S. Børve, H. Sato, H. L. Pécseli, and J. K. Trulsen, Ann. Geophys., 29, 663-671, 2011, doi:10.5194/angeo-29-663-2011

Oscillations with periods on the order of 5-10 min are regularly observed by instrumented spacecrafts in the Earth's magnetosphere. These oscillations often follow sudden impacts related to coronal mass ejections. We demonstrated that a simple model is capable of explaining these oscillations and give a scaling law for their basic characteristics in terms of the basic parameters of the problem. The period of the oscillations and their anharmonic nature, in particular, are accounted for. The model has no free adjustable numerical parameters, but rather attempts to predict some dynamic properties of magnetospheres, on the basis of measurable steady state characteristics. The results agree well with observations. The analysis is supported by numerical simulations solving the Magneto Hydro Dynamic equations in two spatial dimensions, where we let a solar wind interact with a magnetic dipole representing a magnetized Earth. Two tilt-angles of the magnetic dipole axis were considered. We find the formation of a magnetosheath with the magnetopause at a distance corresponding well to the analytical results. Sudden pulses in the model solar wind sets the model magnetosphere into damped oscillatory motions and quantitative agreement with the analytical results is found.

Paper 2:
Fluctuations in the direction of propagation of low frequency ionospheric waves, Hiroatsu Sato, Hans L. Pécseli, Jan K. Trulsen, ESA Publications, Special Publication SP-700, in press.

Low frequency electrostatic waves in the ionospheric E-region are studied using data obtained by an instrumented rocket. Restricting the analysis to low frequencies and long wavelengths we find that the direction of wave-propagation varies randomly within a wide interval of aspect angles. We found evidence for fluctuations, or "jittering", of the direction of the local electric field vector. The distribution of the directional change per time unit is determined. The distribution is found to depend on the intensity of the turbulence indicating also a significant spatial intermittency of the signal. Large amplitude fluctuations have a narrow aspect-angle distribution with little directional fluctuations. The wave properties depend on the strength of the ambient DC-electric field. The analysis is based on a preliminary dataset.

Paper 3:
Experimental studies of low frequency ionospheric waves, H. Sato, H. L. Pécseli, J. K. Trulsen, Proceedings of the ICPIG2011, Belfast, 28th August to 2nd September 2011. In press.

Low frequency electrostatic waves being spontaneously excited in the ionospheric electrojet are studied by instrumented rockets. The data are obtained by four spherical probes placed at two booms in such a way that the probes on the deployed booms form the corners of a tetrahedron. By this construction, the probes can give information of all three vector components of electric fields in the ionosphere. Signals from probe-potential differences are available on ground for further processing. We report results from detailed statistical studies of low frequency long wavelength electric field fluctuations, with particular attention to intermittent features in the data. We find that the largest amplitudes of the fluctuating fields are confined to relatively localized spatial regions. A Gaussian random signal is used as a reference for discussions of the observed intermittency. The analysis is based on a preliminary dataset.

Paper 4:
Fluctuations in the direction of propagation of intermittent low frequency ionospheric waves, H. Sato, H. L. Pécseli, J. K. Trulsen, Submitted for publication 2011

Low frequency electrostatic waves in the ionospheric E-region are studied by using data obtained from an instrumented rocket having four probes mounted on two perpendicular booms. Two data-sets are available, one for up-leg and one for down-leg conditions with somewhat different ionospheric parameters. The ionospheric plasma is unstable with respect to the electrostatic Farley-Buneman instability in both cases, but the DC-electric field is somewhat enhanced during the downleg part of the flight. We find that the direction of wave-propagation as given by the local normalized fluctuating electrostatic field vector varies randomly within an interval of aspect angles. The distribution of the directional change per time unit is determined. The waves propagate predominantly in the electrojet direction, but large variations in aspect angle are found, both with respect to the magnetic field (the aspect angle) and with respect to the electrojet direction. Indications of a significant spatial intermittency of the signal are demonstrated. Large amplitude fluctuations are confined to spatially localized regions and have a narrower aspect-angle distribution with reduced directional fluctuations. We introduce an intermittency measure based on average excess time statistics for the record for the absolute value of the detected time-varying electric fields. The results are compared with a reference obtained from a non-intermittent Gaussian signal. The wave properties and the intermittency features seem to depend on the strength of the ambient DC-electric field. The analytical models for quantifying the intermittency effects were tested by synthetic time series allowing studies of the transition from non-Gaussian to Gaussian random signals.

The author has contributed also to the following paper:

B. Krane, H.L. Pécseli, H. Sato, J. Trulsen and A.W. Wernik, Low-frequency electrostatic waves in the ionospheric E region. Plasma Sources Sci. Technol. 19, 034007, 2010,
doi:10.1088/0963-0252/19/3/034007
This paper is not included here.

Bibliography

Anselmet, F., Y. Gagne, E. J. Hopfinger, and R. A. Antonia, High-order velocity structure functions in turbulent shear flows, *J. Fluid Mech.*, *140*, 63–89, 1984.

Bendat, J. S., *Principles and Applications of Random Noise Theory*, John-Wiley & Sons, New York, 1958.

Boedo, J. A., et al., Transport by intermittency in the boundary of the DIII-D tokamak, *Phys. Plasmas*, *10*, 1670–1677, 2003.

Bowles, K. L., R. Cohen, and B. B. Balsley, Field-aligned E-region irregularities identified with acoustic plasma waves, *J. Geophys. Res.*, *68*, 2485–2501, 1963.

Bruno, R., and V. Carbone, The solar wind as a turbulence laboratory, *Living Rev. Solar Phys.*, *2*, 2005, http://www.livingreviews.org/lrsp-2005-4.

Buneman, O., Excitation of field aligned sound waves by electron streams, *Phys. Rev. Lett.*, *10*, 285–287, 1963.

Chandrasekhar, S., The theory of turbulence, *J. Madras Univ.*, *B27*, 251, 1957.

Chang, T., and C.-C. Wu, Rank-ordered multifractal spectrum for intermittent fluctuations, *Phys. Rev. E.*, *77*, 045,401, 2008, doi:10.1103/PhysRevE.77.045401.

Chen, F. F., Spectrum of low-β plasma turbulence, *Phys. Rev. Lett.*, *15*, 381, 1965.

Chen, F. F., *Introduction to Plasma Physics and Controlled Fusion*, vol. 1, 2 ed., Plenum Press, New York, 1984.

Dyrud, L., B. Krane, M. Oppenheim, H. L. Pécseli, K. Schlegel, J. Trulsen, and A. W. Wernik, Low-frequency electrostatic waves in the ionospheric E-region: a comparison of rocket observations and numerical simulations, *Ann. Geophys.*, *24*, 2959–2979, 2006.

Dyrud, L., B. Krane, M. Oppenheim, H. L. Pécseli, J. Trulsen, and A. W. Wernik, Structure functions and intermittency in ionospheric plasma turbulence, *Nonlin. Processes Geophys.*, *15*, 847–862, 2008.

Farley, D. T., Two-stream plasma instability as a source of irregularities in the ionosphere, *Phys. Rev. Lett.*, *10*, 279–282, 1963.

Farrugia, C. J., and F. T. Gratton, Aspects of magnetopause/magnetosphere response to interplanetary discontinuities, and features of magnetopause Kelvin-Helmholtz waves, *J. Atmospheric Solar-Terrestrial Phys.*, *73*, 40–51, 2011, doi:10.1016/j.jastp.2009.10.008.

Fejer, B. G., and J. F. Providakes, High-latitude E-region irregularities - new results, *Phys. Scripta*, *T18*, 167–178, 1987.

Fejer, B. G., J. Providakes, and D. T. Farley, Theory of plasma waves in the auroral *E* region, *J. Geophys. Res.*, *89*, 7487–7494, 1984.

Fredriksen, A., C. Riccardi, L. Cartegni, D. Draghi, R. Trasarti-Battistoni, and H. E. Roman, Statistical analysis of turbulent flux and intermittency in the nonfusion magnetoplasma Blaamann, *Phys. Plasmas*, *10*, 4335–4340, 2003.

Friker, A., and F.-J. Lübken, Neutral air density and temperature measurements by the TOTAL instrument onboard the ROSE payloads, *J. Atmos. Terr. Phys.*, *54*, 693–701, 1992.

Hinze, J. O., *Turbulence*, 2 ed., McGraw-Hill, New York, 1975.

Huld, T., A. H. Nielsen, H. L. Pécseli, and J. Juul Rasmussen, Coherent structures in two-dimensional turbulence, *Phys. Fluids B*, *3*, 1609–1625, 1991.

Iranpour, K., H. L. Pécseli, J. Trulsen, A. Bahnsen, F. Primdahl, and K. Rinnert, Propagation and dispersion of electrostatic waves in the ionospheric E region, *Ann. Geophys.*, *15*, 878, 1997.

Jackel, B. J., D. R. Moorcroft, and K. Schlegel, Characteristics of very large aspect angle E-region coherent echoes at 933 MHz, *Ann. Geophysicae*, *15*, 54–62, 1997.

Johnsen, H., H. L. Pécseli, and J. Trulsen, Conditional eddies in plasma turbulence, *Phys. Fluids*, *30*, 2239–2254, 1987.

Kelley, M. C., *The Earth's Ionosphere, Plasma Physics and Electrodynamics*, vol. 43 of *International Geophysics Series*, Academic Press, San Diego, California, 1989.

Kelley, M. C., and F. S. Mozer, Electric field and plasma density oscillations due to the high-frequency Hall current two-stream instability in the Auroral E region, *J. Geophys. Res.*, *78*, 2214–2221, 1973.

Kervalishvili, G. N., R. Kleiber, R. Schneider, B. D. Scott, O. Grulke, and T. Windisch, Intermittent turbulence in the linear VINETA device, *Contrib. Plasma Phys.*, *48*, 32–36, 2008.

Kivelson, M. G., J. Etcheto, and J. G. Trotignon, Global compressional oscillations of the terrestrial magnetosphere - the evidence and a model, *J. Geophys. Res.*, *89*, 9851–9856, 1984.

Korotova, G. I., and D. G. Sibeck, A case study of transit event motion in the magnetosphere and in the ionosphere, *J. Geophys. Res.*, *100*, 35–46, 1995.

Krane, B., H. L. Pécseli, J. Trulsen, and F. Primdahl, Spectral properties of low-frequency electrostatic waves in the ionospheric E region, *J. Geophys. Res.*, *105*, 10,585, 2000.

Krane, B., H. L. Pécseli, H. Sato, J. Trulsen, and A. W. Wernik, Low-frequency electrostatic waves in the ionospheric E region, *Plasma Sources Sci. Technol.*, *19*, 034,007, 2010.

Kristensen, L., M. Casanova, M. S. Courtney, and I. Troen, In search of a gust definition, *Boundary-Layer Meteorol.*, *55*, 91–107, 1991.

Olesen, J. K., and J. Rybner, Slant Es disturbance at Godhavn and its correlation with magnetic disturbance, in *AGARDograph*, vol. Ionospheric Research Meeting, pp. 37–57, AGARD Avionics Panel, Cambridge, England, 1958.

Pécseli, H. L., T. Mikkelsen, and S. E. Larsen, Drift wave turbulence in a low β-plasma, *Plasma Phys.*, *25*, 1173–1197, 1983.

Pécseli, H. L., J. Trulsen, F. Primdahl, and A. Bahnsen, Propagation and nonlinear interaction of low-frequency electrostatic waves in the polar cap E region, *J. Geophys. Res.*, *98*, 1603–1612, 1993.

Pfaff, R. F., M. C. Kelley, B. G. Fejer, E. Kudeki, C. W. Carlson, A. Pedersen, and B. Hausler, Electric field and plasma density measurements in the Auroral electrojet, *J. Geophys. Res.*, *89*, 236–244, 1984.

Pfaff, R. F., M. C. Kelley, B. G. Fejer, N. C. Maynard, L. H. Brace, B. G. Ledley, L. G. Smith, and R. F. Woodman, Comparative insitu studies of the unstable daytime equatorial E-region, *J. Atmos. Terr. Phys.*, *47*, 791–811, 1985.

Pfaff, R. F., P. A. Marionni, and W. E. Swartz, Wavevector observations of the two-stream instability in the daytime equatorial electrojet, *Geophys. Res. Lett.*, *24*, 1671–1674, 1997.

Plaschke, F., K.-H. Glassmeier, D. G. Sibeck, H. U. Auster, O. D. Constantinescu, V. Angelopoulos, and W. Magnes, Magnetopause surface oscillation frequencies at different solar wind conditions, *Ann. Geophysicae*, *27*, 4521–4532, 2009.

Rice, S. O., Mathematical analysis of random noise, II, *Bell System Tech. J.*, *24*, 46–156, 1945, reprinted by Wax, N. in: Selected Papers on Noise and Stochastic Processes (1954) Dover, New York.

Rinnert, K., Plasma waves observed in the Auroral E region ROSE campaign, *J. Atmos. Terr. Phys.*, *54*, 683–692, 1992.

Rogister, A., and N. D'Angelo, Type II irregularities in the equatorial electrojet, *J. Geophys. Res.*, *75*, 3879–3887, 1970.

Rollefson, J. P., On Kolmogorov's theory of turbulence and intermittency, *Can. J. Phys.*, *56*, 1426–1441, 1978.

Rose, G., et al., Rocket and Scatter Experiments (ROSE investigations) Final report on the scientific aspects, *Tech. Rep. MPAE-W-40-90-18*, Max-Planck Institute für Aeronomie, 1990.

Rose, G., et al., The ROSE project. Scientific objectives and discussion of first results, *J. Atmos. Terr. Phys.*, *54*, 657–667, 1992.

Shawhan, S. D., *Magnetospheric Plasma Waves*, vol. III of *Solar System Plasma Physics*, chap. III.1.6, pp. 213–270, North-Holland Publishing Company, 1979.

Sibeck, D. G., et al., The magnetospheric response to 8-minute period strong-amplitude upstream pressure variations, *J. Geophys. Res.*, *94*, 2505–2519, 1989.

Tam, S. W. Y., T. Chang, P. M. Kintner, and E. Klatt, Intermittency analyses on the SIERRA measurements of the electric field fluctuations in the auroral zone, *Geophys. Res. Lett.*, *32*, L05,109, 2005, doi:10.1029/2004GL021445.

Tu, C. Y., and E. Marsch, *MHD Structures Waves and Turbulence in the Solar Wind*, Kluwer Academic Publishers, Dordrecht, 1995.

Xu, Y. H., S. Jachmich, R. R. Weynants, and TEXTOR-team, On the properties of turbulence intermittency in the boundary of the TEXTOR tokamak, *Plasma Phys. Contr. Fusion*, *47*, 1841–1855, 2005.

Part II

Papers

I

Paper I

Minute-scale period oscillations of the magnetosphere

S. Børve, H. Sato, H. L. Pécseli and J. Trulsen
Ann. Geophys., **29**, 663-671, 2011,
doi:10.5194/angeo-29-663-2011

Ann. Geophys., 29, 663–671, 2011
www.ann-geophys.net/29/663/2011/
doi:10.5194/angeo-29-663-2011

Annales Geophysicae

Minute-scale period oscillations of the magnetosphere

S. Børve[1,3], H. Sato[2], H. L. Pécseli[2], and J. K. Trulsen[1]

[1]Institute of Theoretical Astrophysics, University of Oslo, Norway
[2]Department of Physics, University of Oslo, Norway
[3]Norwegian Defence Research Establishment (FFI), Norway

Received: 22 February 2011 – Revised: 14 March 2011 – Accepted: 25 March 2011 – Published: 13 April 2011

Abstract. Oscillations with periods on the order of 5–10 min have been observed by instrumented spacecrafts in the Earth's magnetosphere. These oscillations often follow sudden impacts related to coronal mass ejections. It is demonstrated that a simple model is capable of explaining these oscillations and give a scaling law for their basic characteristics in terms of the basic parameters of the problem. The period of the oscillations and their anharmonic nature, in particular, are accounted for. The model has no free adjustable numerical parameters. The results agree well with observations. The analysis is supported by numerical simulations solving the Magneto-Hydro-Dynamic (MHD) equations in two spatial dimensions, where we let a solar wind interact with a magnetic dipole representing a magnetized Earth. We consider two tilt-angles of the magnetic dipole axis. We find the formation of a magnetosheath with the magnetopause at a distance corresponding well to the analytical results. Sudden pulses in the model solar wind sets the model magnetosphere into damped oscillatory motions and quantitatively good agreement with the analytical results is achieved.

Keywords. Magnetospheric physics (Magnetospheric configuration and dynamics)

1 Introduction

The arrival of the pressure increase associated with the interplanetary shock driven by an interplanetary coronal mass ejection (ICME) will compress the low latitude geomagnetic field through an intensification of the Chapman-Ferraro magnetopause current. This leads to a sudden impulse (SI) which can be observed also in low latitude magnetometer records. In a recent publication (Farrugia and Gratton, 2011) it was demonstrated that such SI-events are followed by large amplitude oscillations of ∼5 min periods. These are observed, for instance, by satellites in the cold, dense magnetosheath and in the hot and tenuous magnetosphere plasmas, consistent with other related observations (Plaschke et al., 2009). It has also been found (Kivelson et al., 1984; Sibeck et al., 1989; Korotova and Sibeck, 1995) that magnetic pulsations with 8–10 min periods measured by geosynchronous satellites are well correlated with oscillations in the solar wind dynamic pressure.

It is the purpose of this communication to demonstrate that oscillations at these characteristic periods can be accounted for by a simple model of the magnetosphere. The entire problem of the coupling between the solar wind and the magnetosphere is extremely complicated even under quiet conditions, and will be even more involved during solar wind disturbances. The main purpose of the present work is to reduce the analysis to its bare essentials, and then compare the results with observations and numerical simulations. The present approach is global, while some local models (Samson et al., 1992) study field line resonances associated with Magneto-Hydro-Dynamic (MHD) waveguide modes in the magnetosphere. Other models consider waves propagating in the equatorial plane between the flanks of the bow shock and a turning point deep within the magnetosphere (Harrold and Samson, 1992). Another approach considers the magnetopause surface analogous to an elastic membrane, obtaining its natural modes of oscillation (Freeman et al., 1995).

2 A simple model problem

Assume as a first approximation that the solar wind can be considered as a "wall" of ideally conducting material. Surface currents are induced in the solar wind, in such a way that the Earth's dipolar magnetic field together with the magnetic

Correspondence to: H. L. Pécseli (hans.pecseli@fys.uio.no)

Published by Copernicus Publications on behalf of the European Geosciences Union.

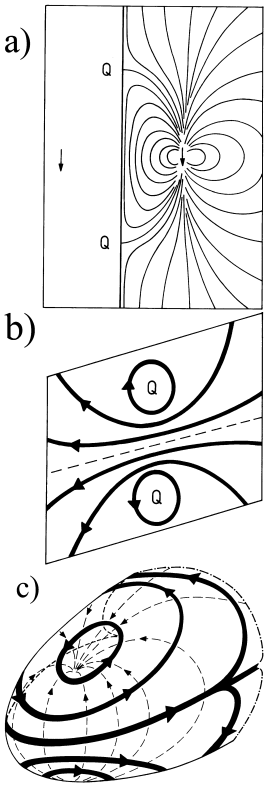

Fig. 1. Simple illustrative model for the magnetosphere, obtained by considering the solar wind as an ideally conducting wall (Chapman and Bartels, 1940; Alfvén, 1950). **(a)** shows the magnetic field lines, and **(b)** selected surface current paths at the interface, being representative for a continuous distribution. The magnetic field vanishes at the cusp-points labeled Q. A schematic illustration of the deformation of the surface of current-paths in **(b)** is shown in **(c)** for a more realistic model.

fields originating from the surface currents cancel inside the model solar wind. This situation is illustrated in Figs. 1a and 1b. For a stationary observer it will appear as if the magnetic field lines near the Earth are "compressed". The magnetic field between the Earth and the ideal solar wind can be determined by the method of images, where an image magnetic dipole is placed inside the solar wind, as indicated by the arrow to the left in Fig. 1a. We will not need this exact solution here, but be content with the overall variation. Note the two cusp points labeled Q on the figure, where the magnetic field intensity vanishes. Using the mirror image and the basic expressions for a magnetic dipole, the construction of Fig. 1a is straight forward. For simplicity we let the magnetic dipole be parallel to the surface of the interface in Fig. 1a, this is a trivial restriction.

The plane surface approximation is only locally valid: the surface containing the current paths is distorted as illustrated in Fig. 1c). The topology of the surface currents is however not changed. The plane surface model can therefore be used as an approximation as the tangent plane at the stagnation point (or "nose region") of the solar wind. The model assumes an ideally conducting solar wind. For large magnetic Reynolds' numbers $R_{\mathrm{L}} \equiv \mu_0 \sigma \mathcal{L} U \gg 1$ the assumptions are applicable even for finite conductivities σ, with $\mathcal{L}$ being a characteristic length-scale for the problem. In our case we estimate $R_{\mathrm{L}} \approx 10^8$. A small magnetic field of $\sim$5 nT embedded in the solar wind is of no significant consequence for the arguments, and will only change the estimate for R_{L} slightly.

2.1 Steady state

We can use the simplified model from Fig. 1 to obtain an estimate for the distance R from the Earth to the stagnation point between the Earth and the Sun (Walker and Russell, 1995). We take the dipolar Earth magnetic field component $B_\theta = \mu_0 \mathcal{M} \sin\theta/(4\pi r^3)$ and derive the magnetic field pressure $B^2/2\mu_0$ at this position. An angle θ between the magnetic dipole axis and the Sun-Earth direction was introduced explicitly, noting that for most relevant cases we have $\theta \approx \pi/2$. With the additional magnetic field contribution from the image dipole, see Fig. 1, we find $B^2/2\mu_0 = 2\mu_0 \mathcal{M}^2 \sin^2\theta/(4\pi r^3)^2$. For stationary conditions, this magnetic pressure has to balance the dynamic pressure from the solar wind. With this latter pressure being the momentum received per sec per unit area, we have the estimate $p = U^2 M n$. We used only the directed momentum density of the solar wind nMU, with M being an average ion mass, and ignored a thermal velocity spread. This can be justified since U is large compared to the sound speed C_s as well as the ion thermal velocity. The net force per unit area on the magnetopause is then

$$F = 2\frac{\mu_0 \mathcal{M}^2 \sin^2\theta}{(4\pi r^3)^2} - nMU^2, \tag{1}$$

where r is a distance in the Earth-Sun direction, as measured from the Earth. For $\theta \approx \pi/2$ we note that the correction due to the tilt of the magnetic dipole is of the order of $(\pi/2-\theta)^2$. This correction is small and will be ignored in the following.

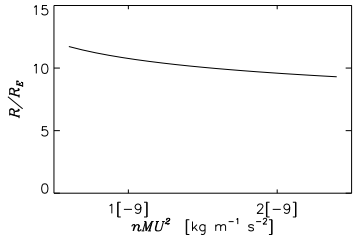

Fig. 2. Normalized Earth-magnetopause distance $R/R_{\rm E}$ for varying dynamic solar wind pressure nMU^2.

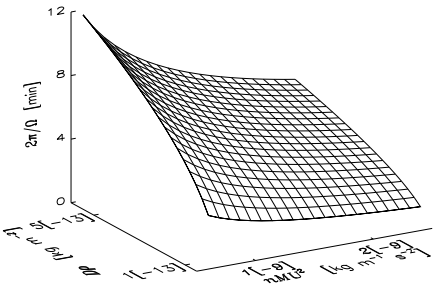

Fig. 3. The period $2\pi/\Omega$ of characteristic small amplitude magnetosphere boundary oscillations for varying solar wind pressure nMU^2 and mass loading $D\rho$.

The equilibrium position R is found by equating the magnetic and solar wind pressures. We find the relation

$$R = \left(\frac{\mu_0 \mathcal{M}^2}{8\pi^2 nMU^2} \right)^{1/6} . \tag{2}$$

Similar expressions can be found in the literature (Walker and Russell, 1995). Inserting typical numbers as $U \approx 3 \times 10^5$ m s^{-1}, $n \approx 5 \times 10^6$ m^{-3}, and the hydrogen mass, $M = 1.66 \times 10^{-27}$ kg, we find $R \approx 7.2 \times 10^7$ m, or $R \approx 11.2\, R_{\rm E}$, in terms of the Earth radius, $R_{\rm E} = 6.4 \times 10^6$ m. The estimate for R is comfortably close to the generally accepted range of $R \sim 10{-}15\, R_{\rm E}$. The model Eq. (2) implies a scaling law for the distance to the magnetosheath boundary in terms of the solar wind velocity U and the solar wind mass density nM. Note that there are no free parameters to fit in Eq. (2).

The numerical values chosen here are somewhat ad-hoc. To illustrate the robustness of the results, we show in Fig. 2 the variability of the normalized Earth-magnetopause distance $R/R_{\rm E}$ for varying solar wind pressures nMU^2. We find that the good agreement with known observational results is robust. It is therefore reasonable to explore also the dynamical properties of this simple model, its natural oscillation period in particular.

2.2 Oscillations without damping

The model discussed here allows for oscillations of the magnetopause around the equilibrium position R. For small, slow displacements of the interface between the solar wind and the magnetosphere, we can assume the solar wind pressure to be constant, while the magnetic pressure varies like $1/r^6$. Assuming small displacements Δ from the equilibrium position R, we will consequently have a net force on the interface given approximately by $F \approx -3\Delta\mu_0\mathcal{M}^2/(4\pi^2 R^7)$. To set up an equation of motion we introduce the mass loading (i.e. mass per unit surface area) of the magnetopause, here written as the product of a thickness D and a mass density ρ to find

$$D\rho \frac{d^2\Delta}{dt^2} = -3\Delta \frac{\mu_0 \mathcal{M}^2}{4\pi^2 R^7}, \tag{3}$$

giving the oscillation period

$$T = \frac{2\pi}{\Omega} = 2\pi \sqrt{\frac{4\pi^2 R^7 D\rho}{3\mu_0 \mathcal{M}^2}} = 2\pi \frac{R}{U} \sqrt{\frac{D\rho}{6nMR}}, \tag{4}$$

using Eq. (2). For simplicity we assume here that the mass density ρ is approximately uniform, while in reality there can be some irregular variations (Song et al., 1990; Gosling et al., 1990).

To estimate the mass loading $D\rho$ giving the inertial term in Eq. (3) we use results from (Spreiter et al., 1966). The importance of the inertia for the problem was recognized also in other studies (Smit, 1968; Freeman et al., 1995). The numerical studies (Spreiter et al., 1966) indicate that typical values are $D \approx R/4$ (consistent with observations by e.g. Song et al., 1990) and $\rho \approx 4nM$. As long as the velocity of the oscillations $d\Delta/dt$ is smaller than the speed of sound, $C_{\rm s}$, we can consider the motion to be incompressible (Landau and Lifshitz, 1987), and therefore let $D\rho$ be constant. (It is easily demonstrated that $d\Delta/dt/C_{\rm s}$ can become large only for large disturbances. In effect, we assume only that $D\rho$ is constant, which is a weaker assumption than strict incompressibility, $\rho \approx$ const.). Inserting the numerical values used before into the analytical result (4) we find a characteristic period to be $2\pi/\Omega = 10.2$ min, which is close to those observed. Within the present model the magnetosphere can be considered as an oscillator which is set into a "ringing" motion by a sudden impulse event. The oscillations are global, and will give detectable signatures also in ground-based instruments measuring magnetic fields, as observed.

In Fig. 3 we illustrate the period of the characteristic magnetosphere boundary oscillations for varying solar wind pressure nMU^2 and mass loading $D\rho$ as defined before. We find characteristic periods in the interval 2–12 min (corresponding to the frequency range 1–8 mHz), which accommodate observations very well (Plaschke et al., 2009). Also we find the results to be robust in the sense that even large variations in one of the parameters only give modest changes in $2\pi/\Omega$. A change in solar wind momentum density changes the equilibrium position, and we have $\Delta R/R \approx -(1/6)\Delta(nMU)/(nMU)$. We emphasize that there are no free parameters to fit in Eq. (3). We use quantities such as D and ρ as inputs, but note that all quantities are amenable to measurements or numerical simulations, so they can not properly be considered as free parameters available for fitting analytical results to observations. Our results in the present work can be seen as an effort to predict some dynamic properties of magnetospheres, on the basis of measurable steady state characteristics.

The simple model outlined here has several features that can be tested experimentally. Due to the strongly anharmonic nature of the restoring force we expect a significant harmonic content. Also the oscillations should have a detectable nonlinear frequency shift.

To discuss the finite amplitude nonlinear case, we rewrite the force without linearization to obtain Newton's second law in the form

$$D\rho\frac{d^2}{dt^2}\Delta = -\frac{\mu_0\mathcal{M}^2}{8\pi^2R^6}\left(1-\frac{1}{(1+\Delta/R)^6}\right), \quad (5)$$

which gives Eq. (3) upon linearization of the right hand side. Introducing the frequency Ω of the small amplitude oscillations we can write Eq. (5) as

$$\frac{d^2}{dt^2}\left(\frac{\Delta}{R}\right) = -\frac{\Omega^2}{6}\left(1-\frac{1}{(1+\Delta/R)^6}\right),$$

or

$$\left(\frac{dZ}{dt}\right)^2 + \frac{\Omega^2}{3}\left(Z+\frac{1}{5(1+Z)^5}-\frac{1}{5}\right) = \Omega^2A^2,$$

with $Z \equiv \Delta/R$ and the right hand side being an integration constant, written in this form for later convenience. The quantity $R\Omega A$ is the velocity of the perturbation at the equilibrium position. By integration we obtain the oscillation period

$$T = \frac{\sqrt{3}}{\Omega}\int_{Z_1}^{Z_2}\frac{dZ}{\sqrt{3A^2-Z-\frac{1}{5(1+Z)^5}+\frac{1}{5}}}, \quad (6)$$

where the integration limits $Z_1 < 0$ and $Z_2 > 0$, with $|Z_1| \neq |Z_2|$, are given as the solutions of $Z-1/5+1/(5(1+Z)^5) = 3A^2$. The amplitude dependence of the normalized variation of the oscillation period is shown in Fig. 4. The nonlinear frequency shift is significant, being up to $\sim 10\%$, and should be observable. The anharmonic features can be made even more conspicuous by considering the velocity and acceleration of the boundary layer, but these quantities can not be detected experimentally, so they are not shown here. We can also demonstrate by a simple Fourier analysis that the oscillations will have a rich harmonic content even for moderate oscillation amplitudes due to the strongly anharmonic nature of the restoring force in Eq. (5). The amplitude of the harmonics is increasing with amplitude A. Harmonics of the magnetospheric oscillations are often observed (Kepko and Spence, 2003).

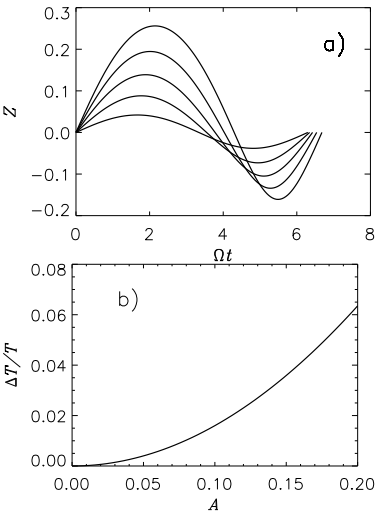

Fig. 4. Numerical solutions of Eq. (5) are shown in **(a)** for five normalized amplitudes $A = 0.04, 0.08, 0.12, 0.16, 0.20$. The normalized nonlinear frequency shift of the characteristic magnetospheric boundary oscillations shown in **(b)** for varying A, where $AR\Omega$ is the reference velocity $d\Delta/dt$ at the position $\Delta = 0$.

2.3 Damped oscillations

The oscillations observed in space are often strongly damped, in variance with the simple model discussed in Sect. 2.2. The following extension of our basic model will account also for a damping mechanism when we take into account that the momentum transferred from the solar wind to the magnetosphere is determined by the *relative* velocities, and not by U alone as assumed in Sect. 2.2. The more general expression for the force (1) can be written as

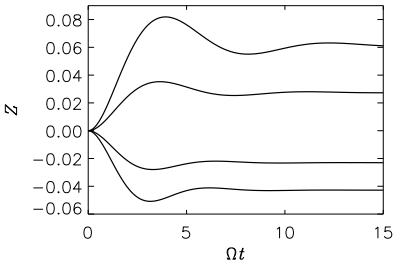

Fig. 5. Numerical solutions of Eq. (9) are shown for four amplitudes $\gamma = \pm 0.15$ and ± 0.30.

$$F = 2\frac{\mu_0 \mathcal{M}^2 \sin^2\theta}{(4\pi(R+\Delta)^3)^2} - nM\left(U + \frac{d\Delta}{dt}\right)^2. \quad (7)$$

Taking again $\theta \approx \pi/2$, expression (5) becomes

$$D\rho\frac{d^2}{dt^2}\Delta = -\frac{\mu_0\mathcal{M}^2}{8\pi^2 R^6}\left(1 - \frac{1}{(1+\Delta/R)^6}\right) - nM\left(2U\frac{d\Delta}{dt} + \left(\frac{d\Delta}{dt}\right)^2\right). \quad (8)$$

In the normalized units used before we have

$$\frac{d^2}{d\tau^2}Z = -\frac{1}{6}\left(1 - \frac{1}{(1+Z)^6}\right) - \frac{2}{\sqrt{6}}\sqrt{\frac{RnM}{D\rho}}\frac{dZ}{d\tau} - \frac{RnM}{D\rho}\left(\frac{dZ}{d\tau}\right)^2, \quad (9)$$

in terms of the normalized time $\tau \equiv \Omega t$. We linearize Eq. (9) to obtain the result

$$\frac{d^2Z}{d\tau^2} = -Z - 2\alpha\frac{dZ}{d\tau}, \quad (10)$$

with the normalized damping coefficient $\alpha \equiv \sqrt{RnM/6D\rho}$. The result (10) has well known solutions in form of damped oscillations $Z(\tau) = \cos(\omega\tau + \delta)\exp(-\tau\alpha)$ with $\omega \equiv \sqrt{1-\alpha^2}$ when $\alpha < 1$. For $\alpha = 1$ we have critical damping, while $\alpha > 1$ gives over-damped oscillations. Small values of α are found when the solar wind speed U is large (giving small R) and the mass loading $D\rho$ is large as well. For most relevant cases we have $\alpha < 1$ but the damping of the oscillations may nonetheless be strong, so that nonlinear effects will be noticeable only for the initial part of the time evolution of a disturbance. The numerical example used in Sect. 2.2 had $RnM = D\rho$ giving $\alpha = 1/\sqrt{6} \approx 0.41$.

A relevant problem to be analyzed by Eq. (9) corresponds to a sudden enhancement of the solar wind plasma density, which we here model by increasing nM while keeping U constant. We use the unperturbed condition for the normalizing quantities and let γ be the fraction of solar wind mass density enhancement. The basic equation can then be written in normalized form as

$$\frac{d^2Z}{d\tau^2} = \frac{1}{6}\frac{1}{(1+Z)^6} - \frac{1}{6}\left(1 + \sqrt{\frac{6RnM}{D\rho}}\frac{dZ}{d\tau}\right)^2(1+\gamma). \quad (11)$$

In Fig. 5 we show numerical solutions of Eq. (11) for different perturbations γ to illustrate the damping of the oscillations. This reference calculation uses $RnM = D\rho$. To illustrate the nonlinear character of the oscillations, we show solutions for both positive and negative changes in the solar wind density. For a linear system, the positive and negative parts of Fig. 5 should be mirror images with respect to the horizontal axis. We expect, however, a different nonlinear response to an increase and a rarefaction in the solar wind. We find that the term containing $(dZ/d\tau)^2$ reduces the damping slightly for realistic amplitudes.

The physical mechanism causing the damping in Eq. (10) is seen to be a phase-lag between the forcing and the displacement of the magnetospheric boundary when it is taken into account that the momentum transfer depends on the solar wind velocity relative to the moving boundary.

3 Numerical simulations

In order to make a qualitative test of the foregoing simple models we carried out some numerical simulations of the interaction of a Solar wind and a magnetic dipole representing the Earth. For simplicity, our simulations are carried out in two spatial dimensions. In this representation, the Earth's magnetic field is modeled not by a small ring current but by two parallel wires, carrying current in opposite directions, perpendicular to the plane of computation. The analytical model refers to the dynamics of the tangent plane at the stagnation point for the solar wind. This plane can be defined for three as well as two-dimensional conditions, but the analytical expressions are slightly different for the two cases.

The numerical methods used are based on a Smooth-Particle-Hydrodynamics (SPH) code solving the Magneto-Hydro-Dynamic (MHD) equations (Monaghan, 1992, 2005; Børve et al., 2005). To generalize the analytical results, we allow the Solar wind to support a weak magnetic field. In this two-dimensional representation, the dipole field becomes

$$\mathbf{B}(\mathbf{r}) = B_E\left(\frac{R_E}{r}\right)^2(\cos\theta\hat{\mathbf{e}}_\theta - \sin\theta\hat{\mathbf{e}}_r) \quad (12)$$

in terms of a reference magnetic field B_E at a reference distance R_E. We note that for this 2-D-model, the magnetic field intensity $|B|$ is independent of θ. We can write the equivalent of Eq. (8) in the form

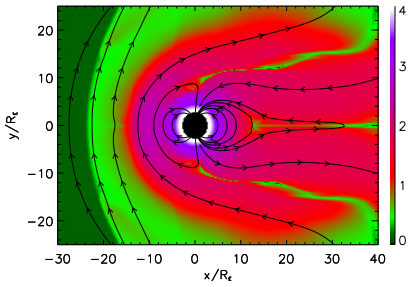

Fig. 6. The magnetic field intensity, here represented by $\ln(|B|+1)$, is shown in color coding with selected magnetic field lines superimposed. Distances are normalized with the Earth radius R_E. See corresponding Fig. 7 for the plasma density. The Sun is in the negative x-direction.

$$D\rho\frac{d^2}{dt^2}\Delta = \frac{2B_E^2}{\mu_0}\left(\frac{R_E}{R}\right)^4\frac{1}{(1+\Delta/R)^4} - nM\left(U+\frac{d\Delta}{dt}\right)^2, \quad (13)$$

where the equilibrium position is

$$R = R_E\left(\frac{2B_E^2}{\mu_0 nMU^2}\right)^{1/4},$$

and the characteristic oscillation period

$$\frac{2\pi}{\Omega} = \frac{2\pi R^{5/2}}{B_E R_E^2}\sqrt{\frac{\mu_0 D\rho}{8}} = 2\pi\frac{R}{U}\frac{1}{2}\sqrt{\frac{D\rho}{RnM}}. \quad (14)$$

A change in solar wind momentum density changes the equilibrium position, and in the present two-dimensional model we have $\Delta R/R \approx -(1/4)\Delta(nMU)/(nMU)$.

In normalized units, the expression (13) becomes

$$\frac{d^2}{d\tau^2}Z = -\frac{1}{4}\left(1-\frac{1}{(1+Z)^4}\right) - \sqrt{\frac{RnM}{D\rho}}\frac{dZ}{d\tau} - \frac{RnM}{D\rho}\left(\frac{dZ}{d\tau}\right)^2. \quad (15)$$

The nonlinear features are less prominent in two spatial dimensions, as seen by comparing the nonlinear term $(1+Z)^{-4}$ in Eq. (15) with $(1+Z)^{-6}$ in Eq. (9). The present two-dimensional results are, however, not significantly different from the model outlined in Sect. 2. Our model is thus robust, and can be tested also with a simplified two-dimensional numerical model as the one used here.

Representative results are shown in Fig. 6 showing the magnetic field intensity represented by $\ln(|B|+1)$ in color coding with selected magnetic field lines superimposed, while Fig. 7 shows the plasma density by $\log_{10}(n)$ with solar wind velocity vectors superimposed. Note the ring-shaped magnetic field intensity near the Earth in Fig. 6, consistent with Eq. (12). A part of the axial variation of the plasma density is shown in Fig. 8. For the numerical results in Figs. 6–8 the positive x-axis (with origin at the Earth) is pointing away from the Sun. The magnetosheath plasma density is larger than in a fully three-dimensional case since the plasma can escape from the stagnation point in two directions only. The distance from Earth to the magnetosheath is approximately $R = 14\,R_E$, in reasonable agreement with predictions of our model.

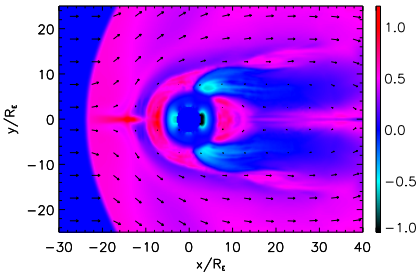

Fig. 7. Variation of the plasma density, here represented by $\log_{10}(n)$, is shown with velocity vectors superimposed. See corresponding Fig. 6 for the magnetic field.

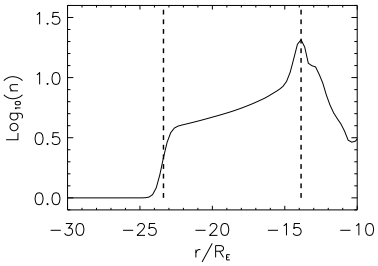

Fig. 8. Variation of plasma density along the line connecting the Sun and the Earth. Distance is normalized also here with the Earth radius R_E. This figure serves to define the positions (shown with vertical dashed lines) of the bow shock (left) and the magnetopause (right) as used later on. The density is normalized by the steady state solar wind plasma density. Note the logarithmic vertical axis. Even small variations of the density can give a large change in the local maximum to the right, so motions of this position are not always well defined.

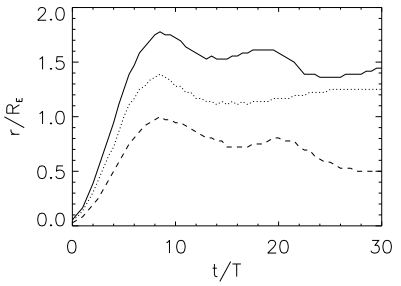

Fig. 9. Bow shock boundary oscillations, see Fig. 8 for definition of the position being considered. The normalizing time is here $T \equiv R_E/U$ where U is the solar wind velocity. We show results for $\Delta n/n = 10\%, 15\%$ and 20%, keeping the solar wind velocity constant. See also Fig. 10.

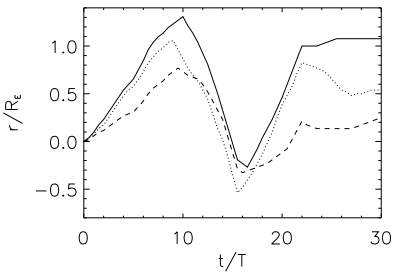

Fig. 10. Magnetopause boundary oscillations corresponding to Fig. 9. See Fig. 8 for definition of the position considered.

When this reference model has reached a steady state, we impose a sudden increase Δn in the solar wind density. The two positions indicated in Fig. 8 are then set in motion. A mechanical equivalent could be a damped spring at rest with a mass load M which at $t = 0$ is hit inelastically by a projectile with mass ΔM, and carrying momentum $U\,\Delta M$. This spring will be set into oscillatory motion until the entire system settles at its new equilibrium state. In Figs. 9 and 10 we show the time variations of the positions of the bow shock and the magnetopause as defined in Fig. 8. The numerical simulations give a smooth density variation between the two boundaries shown in Fig. 8, while observations show irregularities in the density. These probably originate from density variation in the solar wind. The density profile in the simulations changes significantly during the dynamical evolution following the perturbation, so the motion of the local maximum position at the inner boundary at the magnetopause (right hand position indicated in Fig. 8) is not always well defined.

We observe that the magnetosphere is set into damped oscillations, starting at the reference position, oscillating to eventually settle at the new equilibrium position consistent with the new (increased) solar wind pressure. The two positions indicated in Fig. 8 move together in phase, albeit with different amplitudes. We find $\sqrt{RnM/D\rho} \approx 0.5$. The oscillation period is found to be of the order of 11 $R_E/U \approx (11/14)R/U$. This result is within an order of magnitude consistent with Eq. (14), which predicts a period of approximately $2\pi/\Omega = 2\pi R/U$ for the present conditions. The oscillations are damped, with a damping time of 1–2 oscillation periods. From the numerical results we estimate $\alpha = \sqrt{RnM/(4D\rho)} \approx 0.25$, in reasonable agreement with the observed damping time. A nonlinear frequency shift is here barely noticeable, in agreement with the properties of the present two-dimensional model. The results are thus in qualitative agreement with the analytical results of Sect. 2.3 and Fig. 5.

3.1 Simulations with a tilted magnetic dipole

Most of the analysis and the numerical simulations presented so far refer to the case where the magnetic dipole axis is perpendicular to the direction from the Sun to the Earth. The analytical expression (1) allows for a tilt of the magnetic dipole, so formally this simplifying assumption can be relaxed, but the complexity of the problem becomes significantly increased, nonetheless. We can use the numerical simulations to estimate the significance of the assumption of $\theta = \pi/2$. Numerical results are shown in Figs. 11 and 12, to be compared with Figs. 6 and 7 for the magnetic field and density variations, while the time-variations shown in Fig. 13 should be compared with Figs. 9 and 10. We find that all the basic features of the simplified $\theta = \pi/2$ model are recovered, the main difference being that a noticeable phase shift between the oscillating spatial displacement of the two boundaries defined on Fig. 8. We also find a reduction in the equilibrium distance R, consistent with Eq. (2) if a $\sin^2\theta$ correction is included. The average plasma density of the magnetosheath in the simulations is found to decrease with 15–20% when the dipole axis is tilted, while the width D changes only little. The characteristic period of the oscillations is slightly reduced as compared to the case without tilt of the magnetic axis, and the damping time is slightly increased, so that also this observation is in qualitative agreement with our analytical model.

4 Conclusions

We have described a simple model that takes into account the basic features of the interface between the Earth's magnetosphere and the solar wind. We demonstrated how this simple

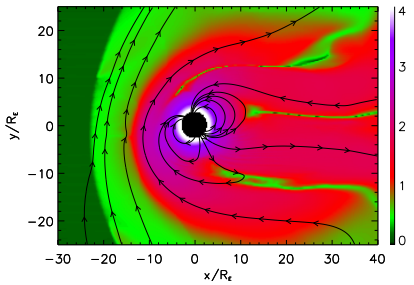

Fig. 11. Magnetic field variations, corresponding to Fig. 6. The present case has a tilt of $\pi/6$ for the magnetic dipole axis.

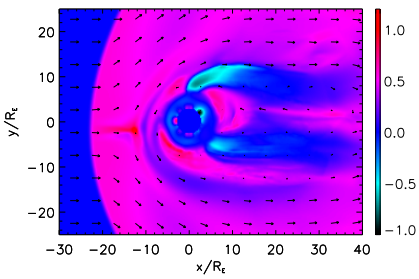

Fig. 12. Density variations corresponding to Fig. 7, here with a tilt of $\pi/6$ for the magnetic dipole axis.

model accounts for the basic characteristics of the distance from the Earth to the magnetosphere boundary and also how the same model accounts for observed characteristic minute scale oscillations often observed in the magnetosphere following SI-events. The observed periods of oscillation can be accounted for. It is also shown how a simple extension of the model explains the damping of the oscillations. Nonlinear effects were included in the analysis, and these can have importance for cases with weakly damped oscillations. We believe that the suggested model can be applied also to other magnetized planets in a solar system.

In support of the analytical model we show results from numerical simulations, obtained for a model system in two spatial dimensions. Good qualitative agreement is found. A sudden change in the solar wind momentum density gives rise to damped oscillations of the boundaries of the computational magnetopause. The simulations demonstrate that the solar wind magnetic field has only minor importance. Its presence will reduce the net magnetic pressure differ-

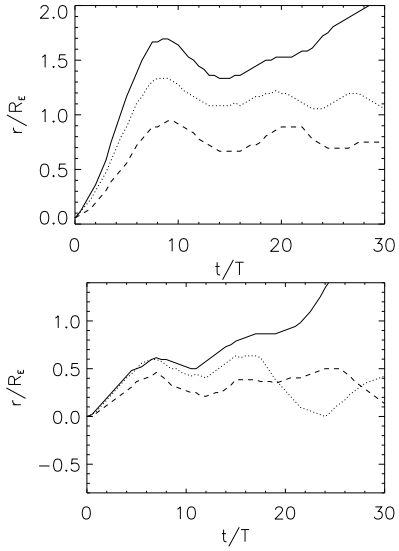

Fig. 13. Figures corresponding to Figs. 9 (top) and 10 (bottom).

ence across the magnetospheric boundary as compared to our model and thus reduce the oscillation frequency. The different amplitudes of the oscillations of the bow shock and the magnetosphere boundary in Figs. 9 and 10 indicate that a more accurate analysis should take into account the compressibility of the magnetospheric plasma, i.e. take into account the time it takes for the perturbation to propagate from the bow shock to the magnetosphere boundary. The relatively strong damping in our simulations makes the nonlinear frequency shift barely noticeable, they might be observable for weaker dampings, i.e. smaller values of $\sqrt{RnM/6D\rho}$.

In the small amplitude limit we have a normalized damping constant $\alpha = \sqrt{RnM/6D\rho}$ which has to be determined by observations or numerical simulations. The damping is very sensitive to changes in α. Quite generally we can state that R is reduced for increasing solar wind velocities. At the same time we expect ρ to increase as well but D to decrease in such a way that $D\rho$ changes only little. At the same time we expect that the natural frequency Ω will increase with U as well so that the normalized damping constant varies as $\sqrt{RnM/6D\rho} \sim U^{-1/3}$ by use of Eq. (2).

By numerical simulation we studied also the importance of the simplifying assumption of $\theta = \pi/2$ in the analysis. Some differences can be noted as already mentioned. Nevertheless

we find the overall features to be well accounted for by the simple model, even for a case where the magnetic dipole axis is tilted by as much as $\pi/6$ with respect to the reference case.

We mention also a possibility for a parametrically driven oscillation for cases where the solar wind pressure is fluctuating. This case can be modeled by setting $U = U(t)$ in Eq. (8), recalling that now also $R = R(t)$. If the power spectrum of the solar wind pressure contains significant energy near Ω, we have the possibility of periodic oscillations sustained for a long time. A similar possibility was mentioned also by Kepko and Spence (2003).

Our ambition here was to obtain the simplest possible model, but point out that many details can be added without much additional effort, such as a dilute plasma in the Earth magnetosphere, and a weak solar wind magnetic field. These additions to the model will contribute to the force balance in relation (1). A tilt of the Earth's magnetic dipole axis is readily accounted for, as demonstrated. The model can be generalized to account also for torsional oscillations where the normal of the local plane of the magnetosphere boundary is turning around a line perpendicular to the Sun-Earth direction. In, for instance, Fig. 1a one of the two lines mentioned is vertical in the plane of the figure, the other one perpendicular to this, out of the paper. Thus, two modes can be identified here, one where the line is parallel to the Earth's magnetic dipole axis and one where it is perpendicular.

Acknowledgements. Valuable discussions with Per Even Sandholt are gratefully acknowledged. We thank Liv Larssen from the Auroral Observatory at the University of Tromsø for helping us by preparing Fig. 1. The project was in part supported by the Norwegian National Science Foundation.

Topical Editor I. A. Daglis thanks one anonymous referee for her/his help in evaluating this paper.

References

Alfvén, H.: Cosmical Electrodynamics, Oxford University Press, London, 1950.

Børve, S., Omang, M., and Trulsen, J.: Regularized smoothed particle hydrodynamics with improved multi-resolution handling, J. Comput. Phys., 208, 345–367, 2005.

Chapman, S. and Bartels, J.: Geomagnetism, Oxford University Press, 1940.

Farrugia, C. J. and Gratton, F. T.: Aspects of magnetopause/magnetosphere response to interplanetary discontinuities, and features of magnetopause Kelvin-Helmholtz waves, J. Atmos. Solar-Terr. Phys., 73, 40–51, doi:10.1016/j.jastp.2009.10.008, 2011.

Freeman, M. P., Freeman, N. C., and Farrugia, C. J.: A linear perturbation analysis of magnetopause motion in the Newton-Busemann limit, Ann. Geophys., 13, 907–918, doi:10.1007/s00585-995-0907-0, 1995.

Gosling, J. T., Thomsen, M. F., Bame, S. J., Onsager, T. G., and Russell, C. T.: The electron edge of low latitude boundary layer during accelerated flow events, Geophys. Res. Lett., 17, 1833–1836, 1990.

Harrold, B. G. and Samson, J. C.: Standing ULF modes of the magnetosphere: A theory, Geophys. Res. Lett., 19, 1811–1814, doi:10.1029/92GL01802, 1992.

Kepko, L. and Spence, H. E.: Observations of discrete, global magnetospheric oscillations directly driven by solar wind density variations, J. Geophys. Res., 10, 1257, doi:10.1029/2002JA009676, 2003.

Kivelson, M. G., Etcheto, J., and Trotignon, J. G.: Global compressional oscillations of the terrestrial magnetosphere – the evidence and a model, J. Geophys. Res., 89, 9851–9856, 1984.

Korotova, G. I. and Sibeck, D. G.: A case study of transit event motion in the magnetosphere and in the ionosphere, J. Geophys. Res., 100, 35–46, 1995.

Landau, L. D. and Lifshitz, E. M.: Fluid Mechanics, vol. 6 of Course of Theoretical Physics, 2 ed., Butterworth-Heinemann, Great Britain, 1987.

Monaghan, J. J.: Smoothed particle hydrodynamics, Annu. Rev. Astron. Astrophys., 30, 543–574, 1992.

Monaghan, J. J.: Smoothed particle hydrodynamics, Rep. Prog. Phys., 68, 1703–1759, 2005.

Plaschke, F., Glassmeier, K.-H., Sibeck, D. G., Auster, H. U., Constantinescu, O. D., Angelopoulos, V., and Magnes, W.: Magnetopause surface oscillation frequencies at different solar wind conditions, Ann. Geophys., 27, 4521–4532, doi:10.5194/angeo-27-4521-2009, 2009.

Samson, J. C., Harrold, B. G., Ruohoniemi, J. M., Greenwald, R. A., and Walker, A. D. M.: Field line resonances associated with MHD waveguides in the magnetosphere, Geophys. Res. Lett., 19, 441–444, doi:10.1029/92GL00116, 1992.

Sibeck, D. G., Baumjohann, W., Elphic, R. C., Fairfield, D. H., Fennell, J. F., Gail, W. B., Lanzerotti, L. J., Lopez, R. E., Lühr, H., Lui, A. T. Y., Maclennan, C. G., Mcentire, R. W., Potemra, T. A., Rosenberg, T. J., and Takahashi, K.: The magnetospheric response to 8-minute period strong-amplitude upstream pressure variations, J. Geophys. Res., 94, 2505–2519, 1989.

Smit, G. R.: Oscillatory motion of the nose region of the magnetopause, J. Geophys. Res., 73, 4990–4993, 1968.

Song, P., Russell, C. T., Gosling, J. T., Thomsen, M., and Elphic, R. C.: Observations of the density profile in the magnetosheath near the stagnation streamline, Geophys. Res. Lett., 17, 2035–2038, 1990.

Spreiter, J. R., Summers, A. L., and Alksne, A. Y.: Hydromagnetic flow around the magnetosphere, Planet. Space Sci., 14, 223–250, doi:10.1016/0032-0633(66)90124-3, 1966.

Walker, R. J. and Russell, C. T.: Introduction to Space Physics, chap. 6: Solar-wind interactions with magnetized planets, pp. 164–182, Cambridge University Press, Cambridge, UK, 1995.

Paper II

II

Fluctuations in the direction of propagation of low frequency ionospheric waves,

Hiroatsu Sato, Hans L. Pécseli, Jan K. Trulsen
ESA Publications Special Publication SP-700, in press

FLUCTUATIONS IN THE DIRECTION OF PROPAGATION OF LOW FREQUENCY IONOSPHERIC WAVES

Hiroatsu Sato[(1)], Hans L. Pécseli[(2)], Jan K. Trulsen[(3)]

[(1)]University of Oslo, Physics Department, Box 1048 Blindern, N-0316 Oslo, Norway. Email: hiroatsu.sato@fys.uio.no
[(2)]University of Oslo, Physics Department, Box 1048 Blindern, N-0316 Oslo, Norway. Email: hans.pecseli@fys.uio.no
[(3)]University of Oslo, Institute of Theoretical Astrophysics, Box 1029 Blindern, N-0315 Oslo, Norway. Email: j.k.trulsen@astro.uio.no

ABSTRACT

Low frequency electrostatic waves in the ionospheric E-region are studied using data obtained by an instrumented rocket. Restricting the analysis to low frequencies and long wavelengths we find that the direction of wave-propagation varies randomly within a wide interval of aspect angles. We found evidence for fluctuations, or ``jittering", of the direction of the local electric field vector. The distribution of the directional change per time unit is determined. The distribution is found to depend on the intensity of the turbulence indicating also a significant spatial intermittency of the signal. Large amplitude fluctuations have a narrow aspect-angle distribution with little directional fluctuations. The wave properties depend on the strength of the ambient DC-electric field.

1. INTRODUCTION

Low frequency longitudinal waves are often spontaneously excited in the ionospheric E-region, in the equatorial as well as the Polar Regions as detected first by radar scattering [1-4] and later by instrumented rockets [5-7].

The Farley-Buneman (FB) instability [2,8-10] excites low frequency electrostatic waves in the E-region of the Earth's ionosphere when the ambient electric field exceeds a certain threshold value, of the order of 20 mV/m. The instability is driven by the Hall-current in the collisional plasma typically found in the ionospheric E-region in the equatorial as well as the polar ionospheres, although the origin of this DC-electric field is generally different in the two regions. We have $\Omega_{ci} \leq \nu_{ni}$ and $\omega_{ce} \gg \nu_{ne}$, with electron and ion cyclotron frequencies ω_{ce} and Ω_{ci}, while the electron and ion neutral collision frequencies are ν_{ne} and ν_{ni}, respectively. The ions are in effect dragged by the neutrals while the electrons on the other hand move approximately with the $\boldsymbol{E}_0 \times \boldsymbol{B}_0/B_0^2$ - velocity. Assuming small growth-rates of the instability, a simplified fluid model gives a linear dispersion relation [11] where the real and imaginary parts of the frequency are

$$\omega_r = \frac{kV_d \cos\alpha}{1+\varphi} \qquad (1)$$

$$\omega_i = \frac{1}{1+\varphi}\left(\frac{\varphi}{\nu_{ni}}(\omega_r^2 - k^2C_s^2) + \frac{\omega_r\nu_{ni}}{kL_n\Omega_{ci}}\right) - 2\beta_r n_0, \qquad (2)$$

where β_r is a recombination coefficient,

$$\varphi = \frac{\nu_{ne}\nu_{ni}}{\omega_{ce}\Omega_{ci}}\left(1 + \frac{\omega_{ce}^2 k_\parallel^2}{\nu_{ne}^2 k^2}\right),$$

and L_n denotes the scale length of a possible large scale plasma density gradient in the direction $\perp \boldsymbol{B}_0$, while $\boldsymbol{V}_d$ is the difference between the electron and ion drift velocities, and α is the angle between $\boldsymbol{V}_d$ and $\boldsymbol{k}$. The analysis uses the quasi-neutrality assumption, and consequently the result only applies for wavelengths much longer than the Debye length, λ_D. The result (1)-(2) is valid in the limit of very small growth rates, $\omega_i \ll \omega_r$, and almost $\mathbf{B}_0$-perpendicular wave propagation, $k_\parallel \ll k_\perp$. We note that a gradient in plasma density contributes to instability at any drift velocity (last term in the parenthesis of (2)) provided it has the correct sign [3]. The relative drift between electrons and ions has to exceed the ion sound speed C_s in order to give Farley-Buneman unstable waves, otherwise the corresponding term has a damping effect. In this simple model, the first waves to become unstable are those where $\boldsymbol{k} \perp \boldsymbol{B}_0$. Since $\omega_{ce} \gg \nu_{ne}$ and $\Omega_{ci} \leq \nu_{ni}$ for the relevant ionospheric conditions, we find that waves with large $k_\parallel$ give large φ and therefore small ω_r, and will consequently remain linearly stable for realistic values of V_d. Recombination acts as a damping mechanism in all cases. For the relevant plasma conditions analyzed in the following, we can ignore large scale plasma density gradients $\perp \boldsymbol{B}_0$. Different models for the linearly unstable dispersion diagram have been compared [12]. We here gave emphasis to the FB and density gradient instabilities, but should mention that also other instabilities can be

operative in the ionospheric E-region, Kelvin-Helmholtz instabilities, for instance. These can be generated by shear in the neutral winds often prevailing in these regions. Finally one can not exclude the possibility that the space-craft itself can generate disturbances to be detected by the probes: such cases can be difficult to identify by a single space-craft.

The aim of the present study is to analyze the direction of the low frequency wave propagation as observed in the ionosphere [13]. Bulk variations in the direction of propagation with altitude were illustrated before [14] together with some earlier qualitative studies [15], but those results were obtained by a local cross correlation, which involves averaging over an altitude interval. Here we want to obtain results with the sampling resolution of the rocket instruments, and analyze also the time variations of the direction of the electric field vector. The present analysis is based on data from the ROSE rocket campaign [15,16]. This communication presents the first results of our analysis as outlined before, as carried out in the fixed rest frame, or ground frame, of reference.

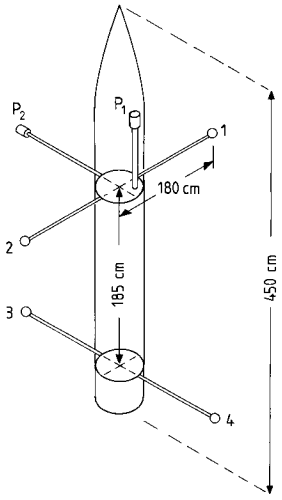

Figure 1. Schematic illustration for the positioning of probes on the ROSE4 rocket [16]. The nose cone is shown intact for illustration.

2. ELECTROSTATIC WAVES OBSERVED IN THE IONOSPHERIC E-REGION

During the ROSE rocket campaign [15,16], an instrumented payload F4 was launched in February 1989 from Kiruna, Sweden. The peak altitude was approximately 125 km. Good quality data were obtained on the up-leg as well as on the down-leg parts of the flight with approximately 20 km horizontal separation. The DC-electric field strength was changing during the flight (typically $\boldsymbol{E}_0 \approx 40$ mV/m up-leg, and $\boldsymbol{E}_0 \approx 60$ mV/m down-leg), so in reality we have data from two independent experiments. The direction and time-variation of $\boldsymbol{E}_0$ is illustrated elsewhere [14,15]. It was found that the *direction* of $\boldsymbol{E}_0$ was relatively constant; the changes were mostly in its amplitude. Numerical simulations of similar ionospheric conditions have also been carried out [12]. In this case a value of $\boldsymbol{E}_0 \approx 70$ mV/m was chosen to emphasize the nonlinear effects.

For completeness we here summarize some of the basic parameters of the flight and the instrumentation. The ROSE F4 rocket was launched in a direction perpendicular to the Hall current of the electrojet. The spin period of the rocket was approximately 0.5 s. The corresponding time for the coning motion was approximately 6 s with cone-angle approximately 2°. The effects of the coning of the rocket can thus be ignored. The rocket payload flew northward. On the upleg part the trajectory made an angle of approximately 30° with respect to the Earth's magnetic field, and was almost parallel with $\boldsymbol{B}$ on the downleg part [15].

The ELF signals analyzed were obtained by gold-plated spherical probes of 5 cm diameter [15], mounted on two pairs of booms, one near the top of the payload (labeled 1 and 2) and the other a distance $L = 185$ cm lower (labeled 3 and 4), oriented at an angle of 90° with respect to the first pair, as illustrated schematically in Fig. 1. The length of each boom was $b = 180$ cm, giving a probe separation of 360 cm on each boom. We analyzed the fluctuating signals $U_6(t) = \phi_1(t) - \phi_2(t)$; $U_5(t) = \phi_4(t) - \phi_3(t)$; $U_4(t) = \phi_1(t) - \phi_4(t)$; $U_3(t) = \phi_2(t) - \phi_3(t)$; $U_2(t) = \phi_1(t) - \phi_3(t)$; and $U_1(t) = \phi_2(t) - \phi_4(t)$, where $\phi_j(t)$ for $j = 1, 2, 3, 4$ denotes the potential on the j-th probe with respect to a suitably defined common ground. There is a redundancy in the available signals, which can be used to check the performance of individual probes. For wavelengths much larger than the probe separations, the potential difference signals can be used to estimate the fluctuating electric fields, $\boldsymbol{E}$. The signals were digitized with 12 bit resolution. The space-time varying electric field fluctuations of the electrojet were originally sampled with a 4 kHz sampling frequency. By averaging sampling points two-by-two, we increase the sampling interval to 0.5 ms, giving a Nyquist frequency of 1000 Hz. The electric circuits give an effective frequency limitation closer to 600 Hz. The DC-electric field $\boldsymbol{E}_0$ was measured by the same probes.

We use a combination of probes to approximate the three electric field components. Thus $U_6/2b$ approximates x-component, $U_5/2b$ the y-component, and $(U_3 + U_4)/2L$ approximates the z-component of the field. For constant electric fields these signals would recover the field-components exactly. For wavelengths longer than the probe separations (as in the present case), we expect this probe combination to give a good approximation for the magnitude and direction of the fluctuating electrostatic field.

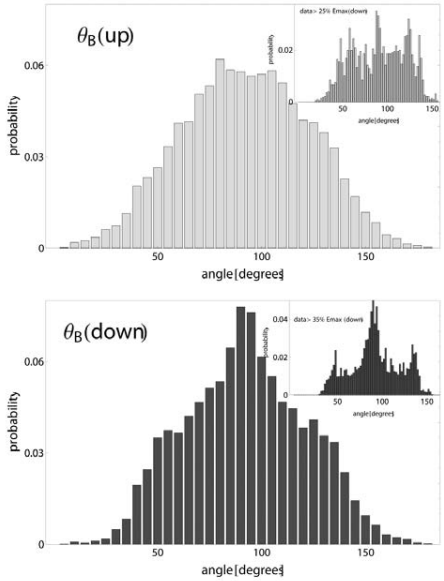

Figure 2. Probability densities of the angle between the electric field vector with respect to $\boldsymbol{B}_0$, for up-leg and down-leg conditions. The figures shown in the inserts are obtained by imposing conditions on the detected field amplitudes.

Studies of the ROSE F4 data demonstrated that a broad band spectrum of low frequency electrostatic waves propagate in the $\boldsymbol{E}_0 \times \boldsymbol{B}_0$-direction with a phase velocity in the range of 250 – 400 m/s. The observed frequency range is 5 – 1000 Hz, implying wavelengths in the range of 0.25 – 80 m. The shortest wavelengths are strongly filtered by the two-point probe sampling of the fluctuating electrostatic fields [14,17,18]. The data approximate the fluctuating electric fields only when the wavelengths significantly exceed the probe separation (see Fig. 1), which here corresponds to frequencies below 28 Hz, approximately. We filter the data correspondingly, and consider only a limited spectral range. (In related previous studies [15], the speed of propagation was not known, and too short wavelengths, i.e. too high frequencies, were included in the data analysis.) We filter the data with a band-pass filter {8:28} Hz, whereby we at the same time remove the rocket spin frequency and its first harmonics, and also ensured that the filter-bandwidth is larger than its average frequency. In case this condition is not fulfilled, the time variability of the output will be determined by the filter characteristics and not the ionospheric signal. Due to the filtering, the present data-set does not contain the ambient electric field $\boldsymbol{E}_0$, nor the $\boldsymbol{V}_R \times \boldsymbol{B}_0$-field, with $\boldsymbol{V}_R$ being the rocket velocity. The variations in magnitude and direction of $\boldsymbol{E}_0$ during the flight are illustrated elsewhere [15].

The electric fields are detected in the rest frame of the rocket. To have the direction in the fixed frame, the data are transformed to a fixed ground frame by use of transformation and rotation matrices. The change in frame of reference is obtained by several such matrix operations. The z-axis is taken to be parallel to the ambient magnetic field.

In Fig. 2 we show the probability density of angles between the electric field vector for the spectral range defined before, as measured with respect to the magnetic field, both for up-leg and down-leg conditions.

For electrostatic waves the direction of the electric field corresponds to the direction of the wave propagation so we can identify a local direction of propagation with the direction of the electric field.

We can obtain results for the directional change with respect to a fixed direction in space, which for these ionospheric conditions is taken to be along $\boldsymbol{B}_0$. The probability density for the variation in electric field direction $\Delta\theta_B$ with respect to $\boldsymbol{B}_0$ from one sampling time step to the next is shown in figure 3.

We can analyze also the changes in direction between $\boldsymbol{E}(t)$ and $\boldsymbol{E}(t+\Delta t)$. The temporal relative variation of the direction of propagation is obtained from the data by the simple formula

$$\Delta\theta_E = ArcCos\left(\frac{\boldsymbol{E}(t)\cdot\boldsymbol{E}(t+\Delta t)}{|E(t)||E(t+\Delta t)|}\right), \quad (3)$$

giving the change in $\theta_E(t)$ within one sampling time interval, Δt. With Δt being small compared to characteristic times for changes in θ_E, we can approximate $\boldsymbol{E}(t+\Delta t) \approx \boldsymbol{E}(t) + \Delta t\ (d\boldsymbol{E}(t)/dt)$, and simplify (3) by a series expansion, which can be used for analytical estimates.

The results for the distribution of θ_E between two directions $\boldsymbol{E}(t)$ and $\boldsymbol{E}(t + \Delta t)$ are shown in Fig. 4. We find that the most probable change in electric field direction within a time interval $\Delta t = 10^{-3}$ s is 2˚- 3˚. For large values of $\Delta\theta_E$, both probability densities can be fitted to a good accuracy by an exponential $\exp(-\Delta\theta_E/\Lambda)$. We find the approximate values $\Lambda = 2.86^{\circ}$ and 3.04° for up-leg and down-leg conditions.

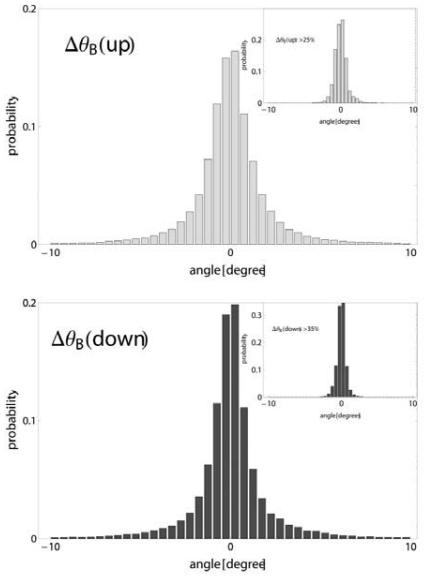

Figure3. Probability densities of the changes in direction of propagation of low frequency electrostatic waves in the ionospheric E-region in the fixed frame of reference. The figure shows the change in direction $\Delta\theta_B$ *with respect to the magnetic field lines within one sampling time* Δt*. To obtain the approximation* $d\theta_B/dt \approx \Delta\theta_B/\Delta t$*, we divide the abscissa values by* $\Delta t = 10^{-3}$ *s.*

To investigate whether observed variations were related to the electric field amplitude we performed a cross correlation between the electric field amplitude and $\Delta\theta_B$, obtaining the values 0.32 and 0.38 for up-leg and down-leg conditions, respectively. This is a nontrivial correlation, which seems to be largest when the ambient electric field E_0 is largest. To test that the finite record length is insignificant for these results we made a test by random number generators, producing synthetic data samples of same length. In this case we found a typical correlation coefficient of the order of 10^{-3}, demonstrating that our results are robust.

3. INTERMITTENT FEATURES OF THE FLUCTUATING ELECTRIC FIELDS

Our basic analysis considers the unconditional electric field direction, i.e. irrespective of the magnitude of $|\mathbf{E}|$. It is known that the signal has significantly intermittent features [19], with localized bursts of intense wave activity intermixed with somewhat more quiescent regions, as illustrated in Fig. 5 showing a sample of $|\boldsymbol{E}(t)|$. The intermittent features are most pronounced for the down-leg part of the flight.

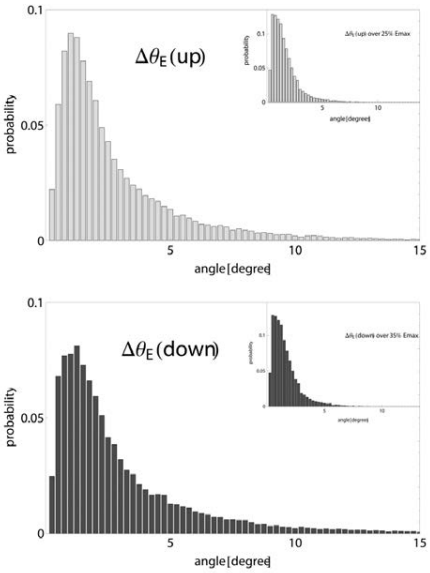

Figure 4. Probability densities of the changes in direction of propagation of low frequency electrostatic waves in the ionospheric E-region. The figure shows $\Delta\theta_E$ *in degrees, as obtained by (3). To obtain the approximation* $d\theta_E/dt \approx \Delta\theta_E/\Delta t$*, we divide the abscissa values by* $\Delta t = 10^{-3}$ *s.*

The results of our analysis changes noticeably if we impose conditions on the magnitude of $|\mathbf{E}|$, as illustrated by inserts in Figs. 2, 3 and 4, where we removed the smallest 35 % of the $|\mathbf{E}|$-values from the analysis (25 % for the upleg part). Now we observe a central peak (seen best on the down-leg part where E_0 was largest) with a moderate aspect angle variation, and an additive distribution of large aspect angle waves. We expect that the central peak represents the Farley-Buneman waves, where both radar [20] and laboratory results [21] give a narrow distribution of aspect angles. Our result for the down-leg part shows a half-width of this central peak

distribution of approximately 7° which is close to previous results [20,22]. Similar results are obtained for the up-leg part of the flight (see Fig. 2), although for this reduced value of E_0 the results are not quite as clear. The time variability of the electric field directions with amplitudes exceeding the 35 % threshold values is also reduced, as evidenced by the inserts in Figs. 3 and 4. This implies that any detection method involving time integration is likely to miss the low amplitude fluctuations, and emphasize the central peak here associated with waves generated by the Farley-Buneman instability. By a Monte-Carlo analysis we find that the angular width obtained by our results is most likely limited by the finite probe separation on the rocket (see Fig. 1), so that the actual angular distribution is likely to be narrower.

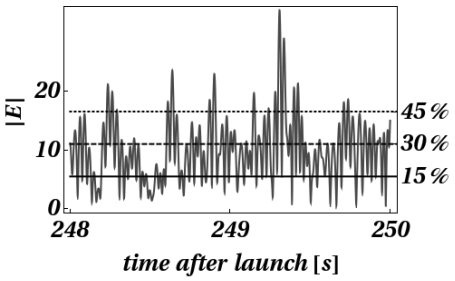

Figure. 5. Illustration of the amplitude-clipping applied for the intermittency studies. Note that the electrostatic waves detected in the ionospheric E-region are not linearly polarized, so it is only rarely that we find the electric field amplitude $|\boldsymbol{E}| = 0$.

We demonstrated also a significant intermittency of the E-region fluctuations: the large amplitude regions contain a significant narrow aspect angle component, which is much less conspicuous in the low amplitude regions. The largest amplitude waves thus seem concentrated into relatively narrow layers that are randomly distributed in altitude. These observation are consistent with the bispectral analysis of the same data as reported before [12,23], where the local bicoherences were found to be of a ``bursty'' nature, concentrated to localized regions. Our results were compared to analytical results for Gaussian random processes, and we confirmed that the intermittency effects observed here originate from non-Gaussian features.

4. DISCUSSIONS AND CONCLUSIONS

In the present study we analyzed the direction of low frequency, long wavelength, electric fields excited in the ionospheric E-region by a cross-field instability. We found that the most probable propagation direction is perpendicular to $\boldsymbol{B}_0$, both for up-leg and down-leg conditions, but note also that deviations in directions as large as 50° have a significant probability of occurrence. The direction of the average wave propagation is, within the uncertainty of the estimate, normal to the DC-electric field [15].

By a conditional analysis, removing the smallest 25 % - 35 % of the electric field amplitudes, we obtained a two-component directional distribution with a central peak here identified with the waves generated by the FB instability. The other component with a wide aspect angle distribution is most likely generated by a different instability, although we are aware of models predicting wide angle distributions for the saturated stage of the FB-instability [24]. A pronounced altitude variation of the propagation velocity was observed for the ROSE F4 data [14], with velocities starting at a value close to the sound speed, but decreasing to noticeably smaller velocities. There are no altitude variations of plasma parameters to explain this variation [14]. In comparison, the propagation velocity obtained by a Greenland rocket [25] under somewhat similar conditions, did not show any significant altitude variation. No significant DC-plasma density variations were detected by the ROSE instruments, so we discard the possibility of density gradient drift waves. The most plausible cause of the altitude variations in the observed propagation velocity is an altitude variation of the neutral wind velocity. The corresponding shear can be a mechanism for generating the waves with wide aspect angle distributions.

Our results indicate a significant intermittency of the long wavelength part of the FB instability, where previous studies [19] refer to the short wavelength part.

Our observations demonstrate a clear difference between the results for up-leg and down-leg conditions. The most significant parameter difference between these two cases is the value of the ambient DC-electric field $\boldsymbol{E}_0$. The rms-fluctuation level varies consistently with $|\boldsymbol{E}_0|$ as demonstrated previously [14,26]. In the present study we have demonstrated that the direction of propagation as determined by the time varying electrostatic field is fluctuating, and found also these fluctuations to be strongest when $|\boldsymbol{E}_0|$ was large. The results can have importance for interpreting the wave vector matching conditions in radar backscatter from instabilities in the ionospheric E-region, for instance.

ACKNOWLEDGMENTS

The Rocket and Scatter Experiment (ROSE) was performed in the framework of the German national sounding rocket program with international participation. It was primarily funded by the Bundes-ministerium für Forschung und Technologie (BMFT) and was managed by the Deutsche Gesellschaft für

Luft- und Raumfahrt (DLR). The present study was supported in part by a grant from the Norwegian National Science Foundation. The authors thank Jean-Pierre St-Maurice for valuable comments.

5. REFERENCES

1. Olesen, J. K. and Rybner, J., In *AGARDograph*, Ionospheric Research Meeting, 37–57, Cambridge, England, September 1958. AGARD Avionics Panel.
2. Bowles, K. L., Cohen, R., and Balsley, B. B., *J. Geophys. Res.,* Vol. 68, 2485–2501, 1963.
3. Balsley B. B., *J. Geophys. Res.,* Vol. 74, 2333–2347, 1969.
4. Olesen, J. K.., In *Radar propagation in the arctic, specialists meeting of the electromagnetic wave propagation*, AGARD-CP-97, page 27, Lindau/Harz, FRG, 13-17, September 1971. Max Planck-Institut für Aeronomie.
5. Prakash, S., Gupta, S. P., Subbaray, B. H., and Jain, C. L., *Nature-Physical Sciences*, Vol. 233, 56-58, 1971.
6. Olesen, J. K., Primdahl, F., Spangslev, F., Ungstrup, E., Bahnsen, A., Fahleson, U., Fälthammar, C.-G., and Pedersen, A., *Geophys. Res. Lett*., Vol. 3, 711–714, 1976.
7. Pfaff, R. F., Kelley, M. C., Fejer, B. G., Maynard, N. C., Brace, L. H., Ledley, B. G., Smith, L. G., and Woodman, R. F., *J. Atmos. Terr. Phys.*, Vol. 47, 791–811, 1985.
8. Farley, D. T., *Phys. Rev. Lett.,* Vol. 10, 279–282, 1963.
9. Buneman, O., *Phys. Rev. Lett.,* Vol. 10, 285–287, 1963.
10. Kelley, M. C., *The Earth's Ionosphere, Plasma Physics and Electrodynamics,*Vol. 43 of International Geophysics Series. Academic Press, San Diego, California, 1989.
11. Fejer, B. G., Providakes, J., and Farley, D. T., *J. Geophys. Res.*, Vol. 89, 7487–7494, 1984.
12. Dyrud, L., Krane, B., Oppenheim, M., Pécseli, H. L., Schlegel, K., Trulsen, J., and Wernik, A. W., *Ann. Geophys*., Vol. 24, 2959–2979, 2006.
13. Pfaff, R. F., Marionni, P. A., and Swartz, W. E., *Geophys. Res. Lett.,* Vol. 24, 1663–1666, 1997.
14. Krane, B., Pécseli, H. L., Trulsen, J., and Primdahl, F., *J. Geophys. Res*., Vol. 105, 10585–10601, 2000.
15. Rinnert, K., *J. Atmos. Terr. Phys.,* Vol. 54, 683–692, 1992.
16. Rose, G., Schlegel, K., Rinnert, K., Kohl, H., Nielsen, E., Dehmel, G., Friker, A., Lubken, F. J., Lühr, H., Neske, E., and Steinweg, A., *J. Atmos. Terr. Phys.*, Vol. 54, 657–667, 1992.
17. Kelley, M. C. and Mozer, F. S., *J. Geophys. Res*., Vol. 78. 2214–2221, 1973.
18. Pfaff, R. F., Kelley, M. C., Fejer, B. G., Kudeki, E., Carlson, C. W., Pedersen, A., and Hausler, B., *J. Geophys. Res.,* Vol. 89, 236–244, 1984.
19. Dyrud, L., Krane, B., Oppenheim, M., Pécseli, H. L., Trulsen, J., and Wernik, A. W., *Nonlin. Processes Geophys.,* Vol. 15, 847–862, 2008.
20. Jackel, B. J., Moorcroft, D. R., and Schlegel, K.., *Ann. Geophysicae*, Vol. 15, 54–62, 1997.
21. Alport, M. J., D'Angelo, N., and Pécseli, H. L., *J. Geophys. Res.,* Vol. 86, 7694–7702, 1981.
22. Jackel, B. J., Moorcroft, D. R, Foster, J. C., and Schlegel, K.., *J. Geophys. Res.,* Vol. 107, 1122, 2002.
23. Larsen, Y., Hanssen A., Krane B., Pécseli H. L., and Trulsen J., *J. Geophys. Res.,* Vol. 107, 1005, 2002, doi:10.1029/2001JA900125.
24. Drexler, J. and St. Maurice, J. P., *Ann. Geophysicae,* Vol. 23, 767–772, 2005.
25. Pécseli, H. L., Primdahl, F., and Bahnsen, A.. *J. Geophys. Res.,* Vol. 94, 5337–5349, 1989.
26. Iranpour, K., Pécseli, H. L., Trulsen, J., Bahnsen, A., Primdahl, F., and Rinnert, K., *Ann. Geophysicae.,* Vol. 15, 878, 1997.

Paper III

III

Experimental studies of low frequency ionospheric waves

H. Sato, H. L. Pécseli, J. K. Trulsen
Proceedings of the ICPIG 2011 28th August to 2nd September (2011). In press

Paper IV

IV

Fluctuations in the direction of propagation of intermittent low frequency ionospheric waves

H. Sato, H. L. Pécseli, J. K. Trulsen
Submitted to JGR for publication 2011